

The impact of ENSO on Southern African rainfall in CMIP5 ocean atmosphere coupled climate models

Dieppois, B. , Rouault, M. and New, M.

Postprint deposited in [Curve](#) February 2016

Original citation:

Dieppois, B. , Rouault, M. and New, M. (2015) The impact of ENSO on Southern African rainfall in CMIP5 ocean atmosphere coupled climate models. *Climate Dynamics*, volume 45 (9): 2425-2442. DOI 10.1007/s00382-015-2480-x

<http://dx.doi.org/10.1007/s00382-015-2480-x>

Springer Berlin Heidelberg

The final publication is available at Springer via <http://dx.doi.org/10.1007/s00382-015-2480-x>

Copyright © and Moral Rights are retained by the author(s) and/ or other copyright owners. A copy can be downloaded for personal non-commercial research or study, without prior permission or charge. This item cannot be reproduced or quoted extensively from without first obtaining permission in writing from the copyright holder(s). The content must not be changed in any way or sold commercially in any format or medium without the formal permission of the copyright holders.

CURVE is the Institutional Repository for Coventry University

<http://curve.coventry.ac.uk/open>

Climate Dynamics

The impact of El Niño on Southern African rainfall in CMIP5 Ocean Atmosphere coupled climate models --Manuscript Draft--

Manuscript Number:	
Full Title:	The impact of El Niño on Southern African rainfall in CMIP5 Ocean Atmosphere coupled climate models
Article Type:	Original Article
Keywords:	Southern Africa; rainfall; El Niño Southern Oscillation (ENSO); coupled model; CMIP5; teleconnection
Corresponding Author:	Bastien Dieppois African Climate & Development Initiative, University of Cape Town Cape Town, Western Cape SOUTH AFRICA
Corresponding Author Secondary Information:	
Corresponding Author's Institution:	African Climate & Development Initiative, University of Cape Town
Corresponding Author's Secondary Institution:	
First Author:	Bastien Dieppois
First Author Secondary Information:	
Order of Authors:	Bastien Dieppois Mathieu Rouault Mark New
Order of Authors Secondary Information:	
Abstract:	<p>We study the ability of 24 Ocean Atmosphere global coupled models from the Coupled Model Intercomparison Project 5 (CMIP5) to reproduce the teleconnections between El Niño Southern Oscillation (ENSO) and Southern African rainfall in austral summer using historical forced simulations, with a focus on El Niño. Overestimations of summer rainfall occur over Southern Africa in all CMIP5 models. Abnormal westward extensions of ENSO patterns are a common feature of all CMIP5 models while the warming of Indian Ocean that happens during ENSO are not correctly reproduced. This could impact the teleconnection between ENSO and Southern African rainfall which is represented with mixed success in CMIP5 models. From the near-surface to mid-troposphere, CMIP5 models underestimate the observed anomalous pattern of pressure occurring over Southern Africa that leads to dry conditions during El Niño years. Large-scale anomalies of suppressed deep-convection over the tropical maritime continent and enhanced convection from the central to eastern Pacific are correctly simulated. However, regional biases occur above Africa and the Indian Ocean, particularly in the position of the South Indian Convergence Zone (SICZ) during El Niño, which can lead to the wrong sign in rainfall anomalies in the northwest part of South Africa.</p>
Suggested Reviewers:	Damian Maurice Lawler, Professor CAWR, Coventry University Damian.Lawler@coventry.ac.uk Yves Richard, Professor CRC, Burgundy University Yves.Richard@u-bourgogne.fr One of the most famous expert in South African climate Nathalie Phillipon, Dr CNRS researcher, CRC, Burgundy University Nathalie.Phillippon@u-bourgogne.fr

	<p>Bruce Hewitson, Professor CSAG, University of Cape Town hewitson@csag.uct.ac.za One of the most famous expert in African climate, and CMIP5 experiments.</p>
--	---

1 **The impact of El Niño on Southern African rainfall in CMIP5 Ocean** 2 **Atmosphere coupled climate models**

3

4 Bastien Dieppois ^{1,2}, Mathieu Rouault ^{2,3}, Mark New ¹5 bastien.dieppois@univ-rouen.fr

6

7 ¹ African Climate & Development Initiative, University of Cape Town, RSA8 ² Department of Oceanography, MARE Institute, University of Cape Town, RSA9 ³ Nansen-Tutu Center for Marine Environmental Research, University of Cape Town, RSA

10

11 **Abstract** We study the ability of 24 Ocean Atmosphere global coupled models from the
12 Coupled Model Intercomparison Project 5 (CMIP5) to reproduce the teleconnections between
13 El Niño Southern Oscillation (ENSO) and Southern African rainfall in austral summer using
14 historical forced simulations, with a focus on El Niño. Overestimations of summer rainfall
15 occur over Southern Africa in all CMIP5 models. Abnormal westward extensions of ENSO
16 patterns are a common feature of all CMIP5 models while the warming of Indian Ocean that
17 happens during ENSO are not correctly reproduced. This could impact the teleconnection
18 between ENSO and Southern African rainfall which is represented with mixed success in
19 CMIP5 models. From the near-surface to mid-troposphere, CMIP5 models underestimate the
20 observed anomalous pattern of pressure occurring over Southern Africa that leads to dry
21 conditions during El Niño years. Large-scale anomalies of suppressed deep-convection over
22 the tropical maritime continent and enhanced convection from the central to eastern Pacific
23 are correctly simulated. However, regional biases occur above Africa and the Indian Ocean,
24 particularly in the position of the South Indian Convergence Zone (SICZ) during El Niño,
25 which can lead to the wrong sign in rainfall anomalies in the northwest part of South Africa.

26 **Keywords** Southern Africa, rainfall, El Niño Southern Oscillation (ENSO), coupled
27 model, CMIP5, teleconnection

28

29

30 **1. Introduction**

31 The El Niño Southern Oscillation (ENSO) can be considered as the leading global climate
32 mode of variability driving interannual rainfall variability in Southern Africa. El Niño events
33 favor droughts in this region (Ropelewski and Halpert 1987 1989; Lindesay 1988; Mason and
34 Jury 1997; Rouault and Richard 2005), especially since the late 1970s (Richard et al. 2000,
35 2001; Phillipon et al. 2012). Recent studies have shown that ENSO effects on South African
36 rainfall respond to interactions between the interannual and synoptic timescales (Pohl et al.
37 2009; Fauchereau et al. 2009). Cook (2001) proposed that ENSO generates atmospheric
38 Rossby waves in the southern hemisphere which could be responsible for an eastward shift of
39 the South Indian Convergence Zone (SICZ), where most of the synoptic-scale bearing
40 systems that affect Southern Africa preferably develop (Todd and Washington, 1999; Todd et
41 al. 2004, Hart et al. 2012a, b). Another hypothesis suggested by Nicholson (1997) and
42 Nicholson and Kim (1997) is that Indian Ocean SST anomalies could shift atmospheric
43 convection and rainfall eastward during El Niño events. A positive pressure anomaly above
44 the continent during El Niño (Mulenga *et al*, 2003) could also affect the diurnal cycle of
45 rainfall in Southern Africa (Rouault et al. 2013).

46

47 Although a number of previous studies have attempted to systematically evaluate the
48 performance of coupled models to simulate the teleconnections between ENSO and tropical
49 rainfall (Joly et al. 2007; Yang and DelSole 2012; Langenbrunner and Neelin 2013; Rowell
50 2013), little has been done to assess the capacity of such models to reproduce the
51 teleconnections between El Niño Southern Oscillation (ENSO) and Southern African rainfall.
52 In this study, we examine the ability of atmosphere-ocean global coupled climate models
53 (AOGCMs) to reproduce observed teleconnections between ENSO and Southern African
54 rainfall with a focus on El Niño using historical runs of the Coupled Model Intercomparison

55 Project 5 (CMIP5). In Section 2, we discuss data, after which we evaluate the ability of
56 coupled models to simulate mean rainfall in Southern Africa and ENSO pattern in the Pacific.
57 Analysis of austral summer El Niño-rainfall teleconnections with a focus on Southern Africa
58 is presented in Section 4. The atmospheric dynamics during El Niño are presented in Section
59 5 and the impact of ENSO on adjacent ocean is presented in Section 6.

60

61 **2. Data**

62 2.1. Observations

63 The Climatic Research Unit (CRU) dataset is used to compare observed and simulated
64 Southern African rainfall. The CRU TS 3.21 rainfall field is produced on a $0.5^\circ \times 0.5^\circ$ grid and
65 is derived from monthly rainfall provided by about 4000 weather stations distributed around
66 the world over the last century (Harris et al. 2014; see also
67 badc.nerc.ac.uk/view/badc.nerc.ac.uk for more explanations on the CRU TS 3.21). We use
68 monthly SST data from the extended reconstructed sea-surface temperature (ERSST) of the
69 National Climatic Data Centre. The ERSST gridded data are generated using in situ data from
70 the Comprehensive Ocean-Atmosphere Data Set and improved statistical methods allowing
71 stage reconstruction using sparse data over a $2.5^\circ \times 2.5^\circ$ resolution grid. The ERSST.v3b
72 version is an improved extended reconstruction and which does not use satellite data (Smith et
73 al. 2008). NCEP/NCAR-1 (NCEP-1) reanalyses are used to infer monthly atmospheric
74 dynamics (Kalnay et al. 1996). Five parameters – meridional (V) and zonal (U) wind, sea-
75 level pressure (SLP), geopotential height at 500 hPa (z500) and calculated outgoing longwave
76 radiation (OLR) are considered here. Note that Camberlin et al. (2001) detected an abrupt
77 shift in NCEP-1 geopotential height and zonal wind over large parts of tropical Africa around
78 1967/68. This artefact may be due to changes in techniques and data used for assimilation.

79

80 2.2. CMIP5 Model output

81 We use 24 individual AOGCMs with a focus on austral summer – December, January and
82 February (DJF) – the core of the Southern African rainy season (Table 1). Data between 1950
83 and 2005 are sourced from the Coupled Model Intercomparison Project (CMIP) using the
84 “historical” experiment from the CMIP phase 5 (CMIP5) database (Taylor et al. 2012). These
85 experiments simulate climate variability and trends from the mid-19th century to the late 20th
86 or early 21st century and are driven by realistic anthropogenic and natural forcing’s (*e.g.* solar,
87 volcanic, sulphate aerosol and greenhouse gas, land use). The initialization schemes are model
88 dependent. For instance, MIROC 5 uses an ocean only initialization schemes (Tatebe et al.
89 2012), while CCSM4 uses ocean and ice initial conditions from an historical experiment
90 (Yeager et al. 2012). The spatial resolution of the various models ranges from 1.125° to 4.5°
91 for the atmosphere component, and from 0.23° to 4.5° for the ocean component. Where an
92 ensemble of simulations for an individual model is available (Table 1), all calculations are
93 performed on each member before showing the overall result as an ensemble average. Finally,
94 a multimodel mean is computed to summarize the results.

95

96 **3. South African rainfall and ENSO variability: CMIP5 vs. Observations**

97 3.1. South African rainfall

98 A monthly rainfall index is calculated over 34°–20°S and 10°–36°E between 1950 and 2005
99 (using land points only for the CMIP5 models). Figure 1a shows the annual cycle of South
100 African rainfall in models and in observations. The models capture correctly the timing of the
101 annual cycle of rainfall but overestimate the annual cycle by 10 to 20 mm per month. By
102 comparing the coefficient of variations, *i.e.* the ratio of the standard deviation to the mean, we
103 examined the performance of the CMIP5 models to reproduce the temporal variance of

104 observed DJF rainfall (Fig. 1b). The amplitude of interannual DJF rainfall variability is lower
105 in all CMIP5 models than in the observations (Fig. 1b).

106

107 The spatial coherency of DJF South African rainfall spatial mean patterns is then investigated
108 using a Taylor diagram (Fig. 1c), which provides a way of graphically summarizing how
109 closely a set of spatial mean patterns match observations. The similarity is quantified in terms
110 of their correlation, their centered root-mean-square difference (RMS) and the amplitude of
111 their variations (represented by their standard deviation [SD]). A reference dataset
112 (observational data; blue square) is plotted along the x-axis. The correlation between model
113 outputs and observation represented by azimuthal angle (dashed lines), and the radial distance
114 (blue dashed circles) from the origin represents the SD (blue circles; Fig. 1c). The distance
115 between each CMIP5 models and observation is proportional to the RMS error after removal
116 of the average (green dashed circles). The spatial mean patterns from CMIP5 experiments are
117 correctly represented, as the spatial correlation between model outputs and observed rainfall is
118 always higher than 0.65, and can reach more than 0.9. The biases related to RMS difference
119 between the simulated and observed spatial mean patterns, which is proportional to the
120 distance to the blue square on the x-axis, are between 0.3 and 1.35 mm per month. The spatial
121 variability (SD) of some CMIP5 models is similar to observation (blue circle), while other
122 models show greater or weaker variations than the observation pattern.

123

124 Figure 2 shows the DJF differences between simulations and observation. As illustrated by
125 the multimodel mean, most of the individual CMIP5 models significantly overestimate DJF
126 rainfall. These overestimations are distributed along a NW-SE direction. Maximal differences
127 are identified over the southeastern coastal regions of Southern Africa, Botswana and
128 Namibia. Meanwhile, some models display a significant underestimation over the north-

129 westernmost regions. It is particularly the case of GISS-E2-R-P1 (Fig. 2l) and INM-CM4
130 models (Fig. 2v). Therefore, although some biases in CMIP5 AOGCMs do occur for Southern
131 African rainfall, these models do reproduce realistic annual cycles and in general correct
132 austral summer rainfall spatial patterns.

133

134 3.2. ENSO variability

135 Several studies (Federov and Philander, 2001; Wittenberg et al. 2006) suggest that accuracy
136 of the mean state is critical for successful ENSO simulation. To obtain an optimal
137 representation of the full ENSO spatial pattern during austral summer, we decompose the
138 tropical Pacific SST (35°S–35°N/120°E–60°W) into unrotated empirical orthogonal functions
139 (EOFs; Preisendorfer 1988) after linearly detrending the data. Principal components (PC)-
140 based indices of the ENSO mode of variability, which contain less noise, are thus calculated
141 between 1950 and 2005. This procedure allows each model, as well as observation, to exhibit
142 their own ENSO patterns, as opposed to an imposed structure given by an index in specific
143 domain (Saji et al. 2006; Cai et al. 2009; Weller and Cai 2013).

144

145 Ability of CMIP5 models to reproduce a correct ENSO pattern is summarized in Figure 3.
146 Figure 3a-b displays the 1st EOF extracted from observation (total fraction of variance about
147 54.36%) and from the multimodel mean of individual CMIP5 models (total fraction of
148 variance about 41.12%). DJF ENSO SST patterns seem correctly reproduced in CMIP5
149 models (Fig. 3b). SST anomalies extending along the equator westward from the South
150 American Coast are surrounded by the classic “horseshoe” pattern of opposite sign.

151

152 The interannual variance of the ENSO indices in the individual CMIP5 models are similar to
153 observations (Fig. 3c), albeit with a slight underestimations in most CMIP5 models. This

154 agrees with Michael et al. (2013) who showed that interannual time-scales of the observed
155 ENSO variability identified by Rasmussen (1991) are nevertheless well reproduced in CMIP5
156 models.

157

158 CMIP5 models also show good skills in reproducing DJF spatial mean patterns of ENSO (Fig.
159 1d). The spatial correlation between model outputs and observed rainfall is always higher than
160 0.6, and can reach more than 0.9 (Fig. 1c). The mean biases are between 0.4 and 0.8°C (Fig.
161 1d). In most of CMIP5 models, the magnitude (SD) of ENSO patterns is however lower than
162 in observation (Fig. 1d). These biases of ENSO patterns are analyzed more objectively and
163 summarized by looking at the differences between the CMIP5 multimodel mean and observed
164 ENSO components (Fig. 1e). According to numerous studies, ENSO CMIP5 patterns exhibit
165 biases in three areas, and were quite prevalent in the CMIP3 experiment (*e.g.*, AchutaRao and
166 Sperber 2006; Capotondi et al. 2006; Lin 2007). The CMIP5 models however display an
167 encouraging 30% reduction of pervasive cold bias in the western Pacific (Bellenger *al.* 2013).
168 Abnormal westward extension of ENSO patterns is a common and main feature of all CMIP5
169 models. These differences between GCMs and observation are characterized by
170 overestimations over the western regions (*i.e.*, locations of the observed “horseshoe”
171 anomalies) and underestimation over the eastern regions (Fig. 1e). Such anomalies are much
172 more pronounced in individual models than in the CMIP5 multimodel mean, and exacerbated
173 in CSIRO-Mk3-6-0, GISS-E2-R-P1 and INM-CM4 (not shown). We note that the warm
174 biases in the equatorial Pacific, resulting in the wrong “double ITCZ” (Lin 2007; Ashfaq et al.
175 2010; Widlansky et al. 2012), are not identified in most CMIP5 models using EOF
176 decompositions, and thus are not observed in the multimodel mean. Underestimation of SST
177 anomalies east of California and Baja peninsula is also identified (Fig. 1e). Such differences
178 are comparatively far less in CNRM-CM5 and MIROC5 (not shown).

179 As proposed by Rowell (2013), such biases in the simulated ENSO variability can impact the
180 teleconnection with Southern African rainfall in three distinct ways: i) erroneous forcing of
181 the atmosphere overlying the oceanic source of the teleconnection, either due to an incorrect
182 response of surface fluxes or boundary layer processes, ii) an erroneous representation of the
183 atmospheric bridge from the oceanic region to the African region and iii) an erroneous rainfall
184 response over some African regions.

185

186 **4. Influence of ENSO on summer South African rainfall**

187 Correlation patterns between PC-based ENSO indices and Southern African rainfall from
188 CMIP5 models and observation are performed and displayed in Figures 3 and 4. Note that the
189 statistical significance is computed according to the Student's *t*-test after re-calculating the
190 degrees of freedom with estimated decorrelation scales.

191

192 We first compare the correlation patterns from observation and, through the multimodel
193 mean, from CMIP5 models (Fig. 3). As proposed by a number of authors (*e.g.*, Ropelewski
194 and Halpert 1987 1989; Lindesay 1988; Mason and Jury 1997; Kruger 1999; Richard et al.
195 2000), significant anti-correlation between ENSO and South African rainfall is detected from
196 the observation (Fig. 3a). El Niño events tend to be associated with dry conditions over
197 Southern Africa (Rouault and Richard 2005). In phase summer relationships, which appear
198 significant between 1982 and 2009 (Philippon et al. 2012), are identified over the Western
199 Cape (Fig. 3a). The CMIP5 multimodel mean highlights a good skill in simulating the anti-
200 correlation over the south-eastern regions, but some uncertainties are identified over the
201 north-eastern regions (Fig. 3b). Meanwhile, finer resolutions of CMIP5 models will be
202 required to capture the relationship between ENSO and Western Cape rainfall.

203 Figure 4 displays the summer-month correlation patterns between ENSO and South African
204 rainfall in the individual CMIP5 models. Statistically, correlation patterns are
205 indistinguishable from random noise in HadGEM2-CC (Fig. 4i) and MRI-CGCM3 (Fig. 4r).
206 Most of the CMIP5 models display a wrong correlation between ENSO and Southern African
207 rainfall over the southwestern and northeastern regions. This is especially the case in
208 ACCESS1-0 (Fig. 4a), CanESM2 (Fig. 4d), CCSM4 (Fig. 4e), FGOALS-g2 (Fig. 4h), IPSL-
209 CM5A-LR and -CM5B-LR (Fig. 4l, n), MRI-ESM1 (Fig. 4s) and all NorESM1 models (Fig.
210 4t-v).

211
212 In summary, CMIP5 biases of South African rainfall seem closely related to differences in
213 simulating ENSO teleconnections. Positive and negative correlation, respectively, between
214 northeastern and southwestern regions could be associated with overestimations and
215 underestimations of northeastern South African and Western Cape rainfall. Better simulations
216 of ENSO-South African rainfall teleconnections are observed where Pacific SST biases are
217 lowest, such as in MIROC5.

218

219 **5. El Niño anomalies of the austral summer atmospheric circulations**

220 5.1. Near-surface circulation anomalies

221 Composite maps of anomalies of sea-level pressures (SLPs) during El Niño events are
222 displayed in Figure 6 for NCEP-1 reanalysis and CMIP5 multimodel mean. Higher than
223 normal pressure in tropical and subtropical regions and lower than normal pressure in
224 temperate regions are observed during El Niño using NCEP-1 reanalysis (Fig. 6a). Higher
225 than normal pressure inhibit rainfall and also lead to a change in general circulation of air
226 masses. High pressure anomalies prevent rainfall in general and could reduce the diurnal
227 cycle of rainfall (Rouault et al. 2012). Changes in general circulation modulate precipitation

228 through their impacts on moisture transport (Rouault et al. 2003, Vigaud et al. 2007, 2009),
229 surface convergence (Cook et al. 2000 2001) and by changing the preferred location of rain
230 bearing systems such as cut-off low (Favre et al. 2012) or Tropical Temperate Trough (Hart et
231 al. 2010 2012a, b; Vigaud et al. 2012; Macron et al. 2014). During El Niño years, both
232 intensification and northward shift of the Santa Helena and Indian Ocean subtropical Highs
233 are documented (Cook et al. 2004; Vigaud et al. 2009). Anomalous high pressure is also
234 identified over the north-eastern part of Southern Africa (Fig. 6a), where rains are associated
235 with the southernmost position of the ITCZ.

236
237 The CMIP5 multimodel mean highlights a good skill in simulating high pressure anomalies in
238 tropical and subtropical regions and low pressure anomalies in temperate regions (Fig. 6a).
239 Underestimations of low pressure anomalies south-east and south-west of Southern Africa,
240 *i.e.*, from the Santa Helena and Mascarene Highs are revealed. Meanwhile the South Atlantic
241 and continental high pressure anomalies are also underestimated. For instance, changes of
242 Santa Helena High pressure system during El Niño are not simulated in BCC-CSM1.1 (Fig.
243 7c), CSIRO-MK3-6-0 (Fig. 7g), GISS-E2-R-P1 (Fig. 7k), IPSL-CM5A-LR or -CM5B-LR
244 (Fig. 7l, n) and INM-CM4 (Fig. 7v). This could explain why dry condition over Southern
245 Africa is not correctly reproduced. High pressure anomalies are too strong over the indo-
246 austral ocean in CCSM4 (Fig. 7a), FGOALS-g2 (Fig. 7h), all NorESM1 models (Fig. 7t-u),
247 and CESM1-WACM (Fig. 7w).

248

249 5.2. Mid-tropospheric circulation anomalies

250 El Niño anomalies of geopotential height at 500 hPa (z500) over the southern hemisphere are
251 displayed in Figure 8 using NCEP-1 reanalysis and the CMIP5 multimodel mean. During El
252 Niño years, anomalous high and low pressures are found over the tropical, subtropical regions

253 and low latitude regions using NCEP-1 (Fig. 8a) and seem to mimic the SLP anomalies. Such
254 anomaly indicates an increase of mid-troposphere pressure gradient over a large part of the
255 southern hemisphere, and is associated with an increase of westerly winds in temperate
256 regions brushing of Southern Africa (Fig. 8a). The high pressure anomalies observed near
257 Namibia and southern Angola act to weaken the continental low (Fig. 8a), and potentially
258 prevent rainfall for the same reason mentioned before. In the Austral Ocean region SLP and
259 z500 anomalies (Fig. 6a, 8a) show an equatorward expansion of mid-latitude westerlies and
260 an increased tendency for drier South Atlantic air-mass to be advected over Southern Africa,
261 consistent with earlier conceptual model of Tyson (1986). However, although westerly are
262 found at lower latitude than normal during ENSO, westerly flow veers southwards after
263 reaching the Southwest Africa. This would create lesser convergence with the oncoming
264 easterly flow from the Indian Ocean which is also weakened, both effect reducing continental
265 convergence of moist air and would decrease rainfall.

266

267 z500 anomalies from CMIP5 models are very similar to that observed in the near-surface, and
268 thus reveal similar mismatch with NCEP-1 reanalysis (Fig. 6-8). Weaknesses in simulating
269 high pressure anomalies are found over the South Atlantic and the Southern African continent
270 (Fig. 8b). Meanwhile, underestimations of low pressure anomalies of Santa Helena and
271 Mascarene High are identified (Fig. 8b). By looking at El Niño composite anomalies from
272 some selected individual CMIP5 models, this would be due to strong intermodel
273 inconsistencies in reproducing the location of such anomalies. Only CNRM-CM5 and
274 MIROC5 clearly display correct anomalies of Santa Helena and Mascarene Highs (not
275 shown). In other models (not shown), these signals are shifted eastward (e.g. INM-CM4),
276 westward (e.g. ACCESS1-0) or southward (e.g. IPSL-CM5A-MR). ENSO related change in
277 the westerly flow is thus correctly reproduced but with regional biases affecting neighboring

278 regions of Southern Africa. Substantial regional inter-model variability of mid-latitude
279 westerly tracks is therefore expected.

280

281 5.3. Large-scale and regional convection anomalies

282 Tropical and extratropical deep convection is estimated using DJF NCEP-1 Outgoing
283 Longwave Radiation (OLR). Strong negative OLR anomalies (in green) are associated with
284 higher than normal clouds while positive anomalies (in grey) refer to suppressed convection
285 (Fig. 9). Southern African summer rainy season is related to negative OLR anomalies (*i.e.*,
286 increase convection) in Southwest Southern Africa extending over the mid-latitudes (Fig. 9a),
287 and can thus be considered as a precursor of tropical-temperate-troughs (TTTs). Indeed, a
288 significant amount of summer rainfall over Southern Africa is attributed to the occurrence of
289 TTTs (Harrison 1984 1986, Hart 2012a, 2012b), During TTT events, convection over the
290 continent is linked to the transients in the mid-latitudes, resulting in the presence of a
291 convective cloud-band and rain elongated along NW-SE direction (Fig. 9a). These TTTs are
292 related to the establishment of the so-called South-Indian Convergence Zone (SICZ in Figure
293 9a; Cook, 2000). Meanwhile, summer rainfall in the northern part of austral Africa and
294 Madagascar are associated with the southernmost position of the ITCZ. We have therefore
295 examined whether these two convective patterns could be sensitive to biases of CMIP5
296 models in simulating the ENSO South African rainfall teleconnection.

297

298 Figure 9b displays composite DJF anomalies of OLR values during El Niño years in the
299 NCEP-1 reanalysis. At the southern hemisphere scale, El Niño years are associated with a
300 west-east contrast of suppressed deep-convection over the maritime continent and enhanced
301 convections from the central to eastern Pacific (Fig. 9b). Suppressed deep-convections are
302 also seen over the South Pacific Convergence Zone and the equatoward-shifted ITCZ (Fig.

303 9b). For Southern Africa, El Niño anomalies are associated with a large band of suppressed
304 convection being surrounded to the east and to the west by enhanced deep-convection both
305 extending in a NW-SE direction (Fig. 9b) suggesting a shift in the SICZ and preferred
306 location of the cloud band. According to Cook (2001), a suppressed convection, probably due
307 to an eastward shift of the SICZ occurs over the northeastern regions of South Africa,
308 Mozambique and South part of Madagascar (Fig. 9b).

309
310 Through a CMIP5 multimodel mean, global anomalous convective pattern are correctly
311 identified (Fig. 9c). However, following the SST biases (Figs. 3 and 11), the CMIP5 models
312 shift westward the enhanced deep-convection from the central to the eastern Pacific (Fig. 9c).
313 This appears to have substantial impact over Southern Africa and Southern part of
314 Madagascar in reducing eastward shift of the SICZ (Fig. 9c). Analysis of OLR composites
315 from individual models confirms such global strengths and regional weaknesses of CMIP5
316 models (Fig. 10). Large-scale anomalous convection patterns are well reproduced over the
317 Pacific Ocean in all CMIP5 models, but with the abnormal westward shift of ENSO patterns.
318 Convection anomalies from Southern Africa and adjacent oceans differ from one model to
319 another. Numerous models show a westward extension of suppressed deep-convection in the
320 ITCZ and Africa, such as ACCESS1-0 (Fig. 10a), BCC-CSM1.1 (Fig. 10c), CanESM2 (Fig.
321 10d), CCSM4 (Fig. 10e), IPSL-CM5B-LR (Fig. 10n), all NorESM1 models (Fig. 10t-u),
322 INM-CM4 (Fig. 10v), CESM1-WACM (Fig. 10w). Eastward shifts of the SICZ do not occur
323 and deep-convection tends therefore to be favored over the northeastern regions of Southern
324 Africa which explained the wrong correlation with ENSO discussed previously. Other
325 models, such as CNRM-CM5 (Fig. 10f), CSIRO-Mk3-6-0 (Fig. 10g), MIROC5 (Fig. 10o),
326 MPI-ESM-P (Fig. 10p) reproduce correctly and underestimate convective anomalies along the

327 ITCZ between Africa and the Indian Ocean. In those models, eastward shifts of SICZ are
328 well-simulated, and suppressed deep-convection is identified over Southern Africa.

329

330 **6. El Niño related SST anomalies**

331 To understand why the ENSO-rainfall teleconnection is not properly represented, we examine
332 the skill of CMIP5 models to reproduce the impact of ENSO on adjacent oceans. In
333 observations, a positive significant correlation between PC-based ENSO indices and Indian
334 Ocean SSTs is identified (Fig. 11a). In other words, the Indian Ocean warms during El Niño
335 and cools during La Nina (Klein et al. 1999). Richard et al. (2000) pointed out that, since
336 1970, El Niño events embedded in a warmer Indian Ocean SST context are associated with
337 dry conditions over Southern Africa, and hypothesize that El Niño and a warmer Indian
338 Ocean collaborate to create subsidence above Southern Africa. Moreover, an eastward shift of
339 the SICZ is forced by warm anomalies in the tropical south Indian Ocean leading to a
340 weakened subtropical high belt at the longitude of Madagascar and a lesser moisture flux
341 towards Southern Africa coming from south of Madagascar. As illustrated through the CMIP5
342 multimodel mean, the change in the Indian Ocean that occurs during ENSO is shifted
343 westward compared to the observed SST pattern (Fig. 11). This is clearly identified in all
344 ACCESS models (Fig. 12a-b), BCC-CSM1.1 (Fig. 12c), CCSM4 (Fig. 12e), FGOALS-g2
345 (Fig. 12h), all NorESM1 models (Fig. 12u-t), INM-CM4 (Fig. 12v), CESM-WACM (Fig.
346 12w). It could be due to the abnormal westward extensions of ENSO modes in most CMIP5
347 models (Fig. 11b). Even more important, outside equatorial latitudes, most of the CMIP5
348 models highlight weaker correlations over the Indian Ocean than in observation (Fig. 11b,
349 12). The warming of Indian Ocean during El Niño event would be much less important in
350 CMIP5 models than in observation. This could explain why eastward shifts of the SICZ are
351 less important in CMIP5 models and why high pressure anomalies are not reproduced by the

352 models. Thus, regarding the Indian SST-ENSO correlation patterns, better matches with
353 observations are identified in CNRM-CM5 (Fig. 12f), MIROC5 (Fig. 12o), all MPI-ESM
354 models (Fig. 12p-q).

355

356 **7. Discussion and Conclusion**

357 This study has provided an overview of the capability of CMIP5 coupled models to represent
358 the impact of ENSO on Southern African summer rainfall. Such teleconnections are
359 influenced by biases in the spatiotemporal variability of ENSO and by an erroneous rainfall
360 response over Southern Africa to ENSO. The CMIP5 experiments show a realistic seasonal
361 rainfall cycle. Interannual variability of rainfall is almost always underestimated while total
362 DJF rainfall is overestimated. Numerous weaknesses in simulating ENSO spatiotemporal
363 variability are still present in most CMIP5 models and do not differ much from CMIP3
364 experiments (*e.g.*, AchutaRao and Sperber 2006; Capotondi et al. 2006; Lin 2007; Bellenger
365 et al. 2013). Especially, westward extensions of ENSO modes of variability are likely to
366 disrupt the atmospheric bridge from the Indo-Pacific region to the South African region.

367

368 As calculated by three metrics in Figure 13, better skill in simulating El Niño dry anomalies
369 throughout South Africa is performed in CNRM-CM5, MPI-ESM-P and, looking through the
370 spatial correlation, in MIROC5. Meanwhile, CMIP5 models with lowest skills, such as
371 CanESM2, IPSL-CM5A-LR and INM-CM4, show anomalous wet conditions northeastern
372 part of Southern Africa. This is due to CMIP5 model shortcomings in simulating ENSO-like
373 anomalies of SLP, deep-convection and SST between the Atlantic and Indian oceans, and
374 more particularly their spatial patterns (Figure 13). From the near-surface to the mid-
375 troposphere, the best CMIP5 models, *i.e.*, CNRM-CM5, HadGEM2-ES and all MPI models,
376 reproduce the shift and change in high pressure affecting the latitudinal location of the mid-

377 latitude westerly tracks over the South Atlantic and South Indian Oceans. The mean relative
378 bias, which is highlighted from models showing standardized biases close to zero in Figure
379 13, affect the shift in pressure over the tropical and subtropical South Atlantic (including the
380 continent) and, thus, could affect the eastward ridging of the Santa-Helena High. Meanwhile,
381 CSIRO-Mk3-6-0, HadGEM2-CC, and CESM1-WACM, which present very odd rainfall
382 patterns, show lowest skills in simulating El Niño SLP anomalies (Fig. 13). In modelling
383 high-pressure over the continent, such odd SLP anomalies can however lead to a false-good
384 reproduction of the ENSO-South African rainfall correlation, for instance in HadGEM2-CC
385 (Fig. 13). Large-scale tropical anomalies of deep-convection over the maritime continent and
386 enhanced convection from the central to eastern Pacific are simulated in CMIP5 models and
387 closely follow the SST biases. Meanwhile, large differences between models occur above
388 Africa and the adjacent oceans due to difficulties in simulating a warm Indian Ocean during
389 El Niño events. Indeed, better skills of CMIP5 models, as seen from CNRM-CM5, all MPI
390 models and MIROC5, occur when eastward shifts of the SICZ and warm Indian SSTs are
391 identified (Fig. 13). The CMIP5 biases therefore affect the longitudinal location of the SICZ,
392 and probably also the position of TTT development. Note however that, although GISS-E2-R-
393 P1 is able to reproduce the warmer Indian SST and the eastward shift of the SICZ,
394 weaknesses in simulating South Atlantic and continental SLP anomalies lead to poor ENSO-
395 rainfall correlation patterns (Fig. 13). This pattern is therefore associated to underestimations
396 of Southern African rainfall in the northernmost regions. The CMIP5 biases in simulating El
397 Niño SLP and z500 anomalies over the South Atlantic might not be linked to anomalies over
398 the Indian Ocean.

399

400

401

402 **Acknowledgments**

403 MR wants to thanks ACCESS, NRF, WRC and the Nansen Tutu for Marine Environmental
404 Research for funding. BD wants to thanks UCT for his URC research fellowship.

405

406 **References**

407 AchutaRao K, Sperber KR (2006) ENSO simulation in coupled ocean-atmosphere models:
408 are the current models better? *Clim Dyn* 27:1–15.

409 Ashfaq M, Skinner CB, Diffenbaugh NS (2010) Influence of SST biases on future climate
410 change projections. *Clim Dyn* 36:1303–1319.

411 Bellenger H, Guilyardi E, Leloup J, Lengaigne M, Vialard J (2013) ENSO representation in
412 climate models: from CMIP3 to CMIP5. *Clim Dyn* 42:1999–2018.

413 Camberlin P, Janicot S, Pocard I (2001) Seasonality and atmospheric dynamics of the
414 teleconnection between African rainfall and tropical sea surface temperature Atlantic vs.
415 ENSO. *Int J Clim* 21:973–1005.

416 Capotondi A, Wittenberg A, Masina S (2006) Spatial and temporal structure of tropical
417 pacific Interannual variability in 20th century coupled simulations. *Ocean Model* 15:274–
418 298.

419 Cai W, Sullivan A, Cowan T (2009) Rainfall teleconnections with Indo-Pacific variability in
420 the WCRP CMIP3 models. *J Clim* 22:5046–5071.

421 Cook KH (2000) The South Indian convergence zone and interannual rainfall variability over
422 Southern Africa. *J Clim* 13:3789–3804.

423 Cook KH (2001) A Southern Hemisphere wave response to ENSO with implications for
424 southern Africa precipitation. *J Atmos Sci* 15:2146–2162.

425 Cook KH (2004) Wet and dry spells within particularly wet and dry summers in the South
426 African summer rainfall region. *Clim Res* 26:17–31.

427 Fauchereau N, Pohl B, Reason CJC, Rouault M, Richard Y (2009) Recurrent daily OLR
428 patterns in the Southern Africa/Southwest Indian Ocean region, implications for South
429 African rainfall and teleconnections. *Clim Dyn* 32:575–591.

430 Favre A, Hewitson B, Tadross M, Lennard C, Cerezo-Mota R (2012) Relationships between
431 cut-off lows and the semiannual and southern oscillations. *Clim Dyn* 38:1473–1487.

432 Federov AV, Philander SG (2001) A stability analysis of the tropical ocean-atmosphere
433 interactions: bridging measurements of, and theory for El Niño. *J Clim* 14:3086–3101.

434 Harris I, Jones PD, Osborn TJ, Lister DH (2014) Updated high-resolution grids of monthly
435 climatic observations - the CRU TS3.10 Dataset. *Int J Clim* 34:623–642.

436 Harrison MSJ (1984) A generalised classification of South African summer rain bearing
437 synoptic systems. *J Climatol* 4:547–560.

438 Harrison MSJ (1986) A synoptic climatology of South African rainfall variations. PhD thesis.
439 University of Witwatersrand, Johannesburg, 341p.

440 Hart NCG, Reason CJC, Fauchereau N (2010) Tropical-extratropical interactions over
441 southern Africa: three cases of heavy summer season rainfall. *Mon Wea Rev* 138:2608–
442 2623.

443 Hart NCG, Reason CJC, Fauchereau N (2012a) Cloud bands over southern Africa:
444 seasonality, contribution to rainfall variability and modulation by the MJO.

445 Hart NCG, Reason CJC, Fauchereau N (2012b) Building a tropical extratropical cloud band
446 metbot. *Mon Wea Rev* 140:4005–4016.

447 Joly M, Voldoire A, Douville H, Terray P, Royer J-F (2007) African monsoon
448 teleconnections with tropical SSTs : validation and evolution in a set of IPCC4
449 simulations. *Clim Dyn* 29:1–20.

450 Kalnay E, Kanamitsu M, Kistler R, Collins W, Deaven D, Gandin L, Iredell M, Saha S,
451 White G, Woolen J, Zhu Y, Chelliah M, Ebisuzaki W, Higgins W, Janowiak J, Mo KC

452 Ropelewski C, Wang J, Leetma R, Reynolds R, Jenne R, Joseph D (1996) The
453 NCEP/NCAR 40-year reanalysis project. *Bull Amer Met Soc* 77:437–471.

454 Klein SA, Soden BJ, Lau NC (1999) Remote sea surface variations during ENSO: evidence
455 for a tropical atmospheric bridge. *J Clim* 12:917–932.

456 Kruger, A.C. (1999). The influence of the decadal-scale variability of summer rainfall on the
457 impact of El-Niño and La Niña events in South Africa. *Int J Clim* 19:59–68.

458 Langenbrunner B, Neelin DJ (2013) Analyzing ENSO teleconnections in CMIP models as a
459 measure of model fidelity in simulating precipitation. *J Clim* 26:4431–4446.

460 Lin J-L (2007) The double-ITCZ problem in IPCC AR4 coupled GCMs: Ocean-atmosphere
461 feedback analysis. *J Clim* 20:4497–4525.

462 Lindesay JA (1988) South African rainfall, the souther oscillation and a souther hemisphere
463 semi-annual cycle. *J Climatol* 8:17–30.

464 Macron C, Pohl B, Richard Y (2014) How do Tropical Temperate Troughs Form and Develop
465 over Southern Africa? *J Clim* 27:1633–1647.

466 Mason SJ, Jury M (1997) Climatic variability and change over the Southern Africa: a
467 reflection on underlying processes. *Prog Phys Geo* 21:23–50.

468 Michael J-P, Misra V, Chassignet EP (2013) The El Niño and Southern Oscillation in the
469 historical centennial integrations of the new generation of climate models. *Reg Environ*
470 *Change* 13:121–130.

471 Mulenga HM, Rouault M, Reason CJC (2003) Dry summers over north-eastern South Africa
472 and associated circulation anomalies. *Clim Res* 25:29-41.

473 Nicholson SE (1997) An analysis of the ENSO signal in the tropical Atlantic and western
474 Indian oceans. *Int J Clim* 17:345–375.

475 Nicholson SE, Kim J (1997) The relationship of the El Niño-Southern Oscillation to African
476 rainfall. *Int J Clim* 17:117–135.

477 Pohl B, Fauchereau N, Richard Y, Rouault M, Reason CJC (2009) Interactions between
478 synoptic, intraseasonal and Interannual convective variability over Southern Africa. *Clim*
479 *Dyn* 33:1033–1050.

480 Phillipon N, Rouault M, Richard Y, Favre A (2012) The influence of ENSO on winter rainfall
481 in South Africa. *Int J Clim* 32:2333–2347.

482 Preisendorfer RW (1988) *Principal Component Analysis in Meteorology and Oceanography*.
483 Elsevier, Amsterdam.

484 Rasmusson EM (1991) Observational aspects of ENSO cycle teleconnections. In:
485 *Teleconnection Linking Worldwide Climate anomalies: Scientific Basis and Societal*
486 *Impact* [Glantz et al. (eds.)]. Cambridge University Press, United Kingdom and New
487 York, 309–343.

488 Richard Y, Trzaska S, Roucou P, Rouault M (2000) Modification of the Southern African
489 rainfall variability/El Niño southern oscillation relationship. *Clim Dyn* 16:883–895.

490 Richard Y, Fauchereau N, Pocard I, Rouault M, Trzaska S (2001) XXth century droughts in
491 Southern Africa: spatial and temporal variability, teleconnections with oceanic and
492 atmospheric conditions. *Int J Clim* 21:873–885.

493 Ropelewski CF, Halpert MS (1987) Global and regional scale precipitation patterns
494 associated with the El Niño/Southern Oscillation. *Mon Wea Rev* 115:1606–1626.

495 Ropelewski CF, Halpert MS (1989) Precipitation patterns associated with the high indices
496 phase of the southern oscillation. *J Clim* 2:268–284.

497 Rouault M, Florenchie P, Fauchereau N, Reason CJC (2003) South East tropical Atlantic
498 warm events and southern African rainfall. *Geophys Res Lett* 30:8009.
499 Doi:10.1029/2002GL014840.

500 Rouault M, Richard Y (2005) Intensity and spatial extent of droughts in Southern Africa.
501 *Geophys Res Lett* 32:L15702. Doi:10.1029/2005GL022436.

502 Rouault M, B. Pohl, Penven P (2010) Coastal Oceanic climate change and variability from
503 1982 to 2009 around South Africa. *S Afr J Mar Sci* 32(2): 237–246.

504 Rouault M, Sen Roy S, Balling JRC (2013) The diurnal cycle of rainfall in South Africa in the
505 austral summer. *Int J Clim* 33:770–777.

506 Rowell DP (2013) Simulating SST Teleconnections to Africa: What is the state of the Art? *J*
507 *Clim* 26:5397–5418.

508 Saji N, Xie S-P, Yamagata T (2006) Tropical Indian Ocean variability in the IPCC twentieth-
509 century climate simulations. *Journal of Climate* 19:4397–4417.

510 Smith T, Reynolds R, Peterson TC, Lawrimore J (2008) Improvements to NOAA’s historical
511 merged land-ocean surface temperature analysis (1880-2006). *J Clim* 21:2283–2296.

512 Tatebe H, Ishii M, Mochizuki T, Chikamoto Y, Sakamoto T, Komuro Y, Mori M, Yasunaka,
513 S, Watanabe M, Ogochi K, Suzuk, T, Nishimura T, Kimoto M (2012) Initialization of the
514 climate model MIROC for decadal prediction with hydrographic data assimilation. *J*
515 *Meteorol Soc Jpn*, 90A:275–294.

516 Taylor KE (2001) Summarizing multiple aspects of model performance in a single diagram. *J*
517 *Geophys Res-Atmos* 106:7183–7192.

518 Taylor KE, Stouffer RJ, Meehl GA (2012) An Overview of CMIP5 and the experiment
519 design. *Bull Amer Meteor Soc* 93:485–498.

520 Todd MC, Washington R (1999) Circulation anomalies associated with tropical-temperate
521 troughs in southern Africa and the southwest Indian Ocean. *Clim Dyn* 15:937–951.

522 Todd MC, Washington R, Palmer PI (2004) Water vapour transport associated with tropical-
523 temperate trough systems over Southern Africa and the southwest Indian Ocean. *Int J*
524 *Clim* 24:555–568.

525 Tyson PD (1986) Climatic change and variability in Southern Africa. Oxford University
526 Press, Cape Town.

527 Vigaud N, Richard Y, Rouault M, Fauchereau N (2007) Water vapour transport from the
528 tropical Atlantic and summer rainfall in tropical southern Africa. *Clim Dyn* 28 (2-3): 113–
529 123.

530 Vigaud N, Richard Y, Rouault M, Fauchereau N (2009) Moisture transport between the South
531 Atlantic Ocean and southern Africa: relationships with summer rainfall and associated
532 dynamics. *Clim Dyn* 32:113–123.

533 Vigaud N, Pohl B, Crétat J (2012) Tropical-temperate interactions over Southern Africa
534 simulated by a regional climate model. *Clim Dyn* 39:2895-2916.

535 Ward (1992) Provisionally correctly surface wind data, worldwide ocean-atmosphere surface
536 fields and Sahelian rainfall variability. *J Clim* 5:454–475.

537 Weller E, Cai W (2013) Asymmetry in IOD and ENSO Teleconnection in a CMIP5 Model
538 Ensemble and Its Relevance to Regional Rainfall. *J Clim* 26:5139–5149.

539 Widlansky MJ, Timmermann A, Stein K, McGregor S, Schneider N, England MH, Lengaigne
540 M, Cai W (2012) Changes in South Pacific rainfall bands in a warming climate. *Nature*
541 *climate change* 3:417–423.

542 Wittenberg AT, Rosati A, Lau N-C, Ploshay JJ (2006) GFDL's CM2 global coupled climate
543 models. Part III: tropical Pacific climate and ENSO. *Journal of Climate* 19:698–722.

544 Yang X, DelSole T (2012) Systematic comparison of ENSO teleconnection patterns between
545 models and observations. *J Clim* 25:425–446.

546 Yeager S, Karspeck A, Danabasoglu G, Tribbia J, Teng H (2012) A decadal prediction case
547 study: Late twentieth-century North Atlantic Ocean heat content. *J Clim* 25:5173-5189.

548 Zhang GJ, Wang H (2006) Toward mitigating the double ITCZ problem in NCAR CCSM3.
549 *Geophys Res Lett* 33:L06709. doi:10.1029/2005GL025229.

550

551

552

553 **Figure and Captions**

554

555 **Table 1.** Summarized information on observation data and CMIP5 models used in the study.

556

557 **Fig 1.** Evaluation of model performances. **a** Annual cycle of Southern African rainfall (36°–
558 20°S, 10°–36°E) from CRU TS 3.21 observations (blue), CMIP5 models (grey) and
559 multimodel mean (MMM; red). **b** Coefficient of variation of DJF rainfall time-series from
560 CMIP5 models (grey), the multimodel mean (MMM, red) and observation (blue) over South
561 African region. **c** Taylor diagram of the DJF rainfall spatial patterns from the CMIP5-MMM
562 (red), 24 individual models (grey) and from observations (blue square) over the tropical
563 Pacific. The diagram is a function of the root mean square (RMS, green dashed circles – x-
564 axis), the correlation coefficient (black dashed lines – y-axis) and the standard deviation (blue
565 dashed compared to solid circles – x-axis). Since the values are normalized the reference
566 (observation values) has a standard deviation of 1.

567

568 **Fig. 2** Summer (DJF) differences between simulated and observed rainfall fields (mm/day)
569 between 1950 and 2005. **a** the CMIP5 multimodel mean (MMM) minus the CRU TS 3.21
570 observations. **b** Idem for the 24 individual models from CMIP5 experiments. The statistical
571 significance of differences (red dashed contours) has been estimated using a Student *t*-test at
572 $p=0.05$.

573

574 **Fig. 3** Summer (DJF) ENSO SST mode of variability between 1950 and 2005: CMIP5-MMM
575 vs observations. Empirical Orthogonal Functions (EOFs) of DJF Pacific SSTs using **a** CMIP5
576 multimodel mean (MMM), **b** ERSST.v3b observation and **c** the difference between the two. **c**
577 Standard deviation of DJF-ENSO principal components (PCs) extracted by EOFs from the
578 CMIP5-MMM (red), 24 individual models (grey) and from observations (blue) over the
579 tropical Pacific, **d** Taylor diagram of the ENSO patterns from the CMIP5-MMM (red), 24
580 individual models (grey) and from observations (blue square) over the tropical Pacific. The
581 diagram is a function of the root mean square (RMS, green dashed circles – x-axis), the
582 correlation coefficient (black dashed lines – y-axis) and the standard deviation (blue dashed
583 circles compared to solid circle – x-axis). Since the values are normalized the reference
584 (observation values) has a standard deviation of 1.

585

586 **Fig. 4** Observed and simulated DJF correlations between ENSO and South African rainfall. **a**
587 pointwise correlation between the ENSO component extracted by EOF and South African
588 rainfall in observation and **b** the CMIP5 multimodel mean (MMM). Red dashed contours
589 indicate the 90% confidence level of Pearson's product moment correlation coefficient
590 assuming independent normal distributions.

591

592

593 **Fig. 5 a-x** Simulated DJF pointwise correlation between the ENSO component extracted by
594 EOF and South African rainfall in the individual models from CMIP5 experiments. Red
595 dashed contours indicate the 90% confidence level of Pearson's product moment correlation
596 coefficient assuming independent normal distributions.

597

598 **Fig. 6** Observed and simulated El Niño summer anomalies of the surface atmospheric
599 circulation near South Africa. El Niño composite anomalies (*i.e.*, ENSO-PC>0.01) of Sea
600 Level Pressures (in mb) **a** NCEP-1 reanalysis and **b** CMIP5 multimodel mean (MMM). The
601 statistical significance (red dashed contours) has been estimated using a *t*-test at $p=0.05$. This
602 test is applied on zonal and meridional winds for the NCEP-1 composite map.

603

604 **Fig. 7** SLP summer anomalies near South Africa during El Niño years in the individual
605 CMIP5 models between 1950 and 2005. **a-x** Niño composite anomalies (*i.e.*, ENSO-PC>0.01)
606 of SLPs (in mb) in the individual models from historical runs of CMIP5 models. The
607 statistical significance (red dashed contours) has been estimated using a *t*-test at $p=0.05$.

608

609 **Fig. 8** Observed and simulated El Niño summer anomalies of mid-tropospheric atmospheric
610 circulation over the southern hemisphere. El Niño composite anomalies (*i.e.*, ENSO-PC>0.01
611 of z500 (in m) **a** NCEP-1 reanalysis, **b** CMIP5 multimodel mean (MMM) and **c-f** some
612 selected individual models. Wind anomalies (vectors, $m.s^{-1}$) are only displayed for NCEP-1.
613 The statistical significance (red dashed contours) has been estimated using a *t*-test at $p=0.05$.
614 This test is applied on zonal and meridional winds for the NCEP-1 composite maps.

615

616 **Fig. 9** Outgoing longwave radiations (OLR) anomalies during austral summer to OLR
617 anomalies during El Niño events. **a** Composite anomalies of OLR (in $W.m^{-2}$) during austral
618 summer rainfall in South Africa (*i.e.*, DJF rainfall > 1.75mm/month). **b** El Niño composite
619 anomalies (*i.e.*, ENSO-PC>0.01) of OLR **b** in the NCEP-1 reanalysis and **c** in the CMIP5
620 multimodel mean (MMM). The statistical significance (red dashed contours) has been
621 estimated using a *t*-test at $p=0.05$.

622

623 **Fig. 10** El Niño summer anomalies of OLR over the southern hemisphere in the individual
624 CMIP5 models. **a-x** El Niño composite anomalies (*i.e.*, ENSO-PC>0.01) of OLR (in $W.m^{-2}$)
625 in the individual CMIP5 models. The statistical significance (red dashed contour lines) has
626 been estimated using a *t*-test at $p=0.05$.

627

628 **Fig. 11** Observed and simulated DJF correlations between ENSO components and worldwide
629 SSTs. **a** pointwise correlation between the ENSO components extracted by EOF and SSTs in
630 observation and **b** CMIP5 multimodel mean (MMM). Grey contours indicate the 90%
631 confidence level of Pearson's product moment correlation coefficient assuming independent
632 normal distributions.

633

634 **Fig. 12** DJF correlations between ENSO components and worldwide SSTs hemisphere in the
635 individual CMIP5 models. **a-x** Pointwise correlation between the ENSO component extracted
636 by EOF and SSTs in the individual CMIP5 models. Grey contours indicate the 90%
637 confidence level of Pearson's product moment correlation coefficient assuming independent
638 normal distributions.

639

640 **Fig. 13.** Ranking of CMIP5 models based on the performances in simulating the different
641 aspects of ocean-atmospheric dynamics related to El Niño-Southern African rainfall
642 teleconnections, and also rainfall over Southern Africa itself. Three metrics quantifying the
643 biases from observations are applied to ENSO-rainfall correlation patterns (36–20°S; 10–
644 38°E), SLP anomalies (0–55°S; 20°W–80°E), OLR anomalies (0–55°S; 20°W–80°E) and
645 ENSO-Indian SST correlation patterns (35°S–30°N; 30°120°E). CMIP5 biases are assessed
646 through the deviations from perfect scores: i) one minus the spatial correlation coefficients
647 between observed and simulated patterns (1-R); ii) since the observed values are normalized
648 (SD=1), the absolute values of one minus the standard deviations of CMIP5; and iii) the root
649 mean square error (RMSE). Each row in the table is then individually standardized to
650 compare the CMIP5 models. Blue (red) squares indicate models showing lower (higher) bias
651 than the multimodel mean. Rank of each model also is displayed for each measurement in the
652 bottom left corner, while all the models are displayed from their general ranking from the left
653 to the right.

Figure 1
[Click here to download high resolution image](#)

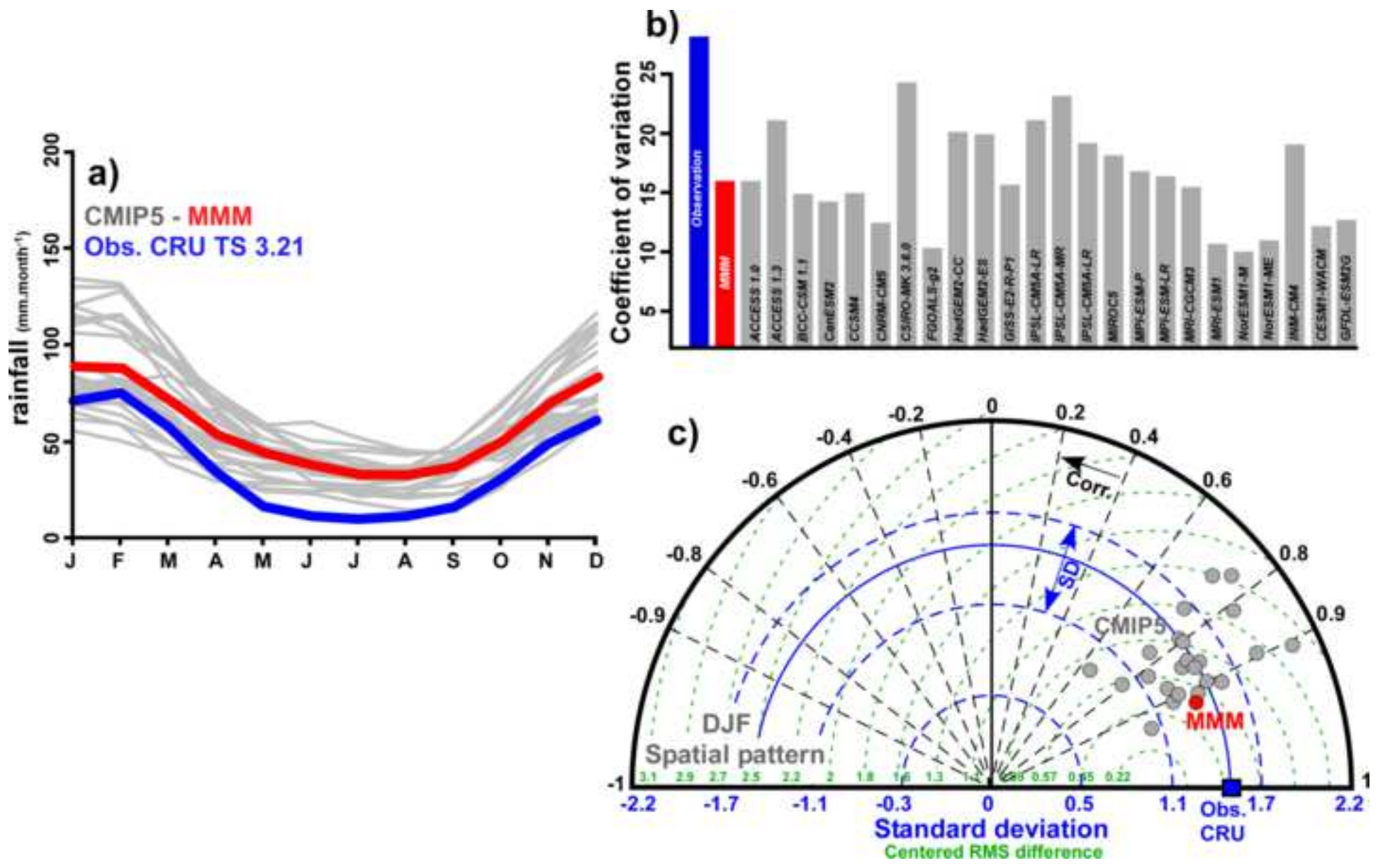


Figure 2
[Click here to download high resolution image](#)

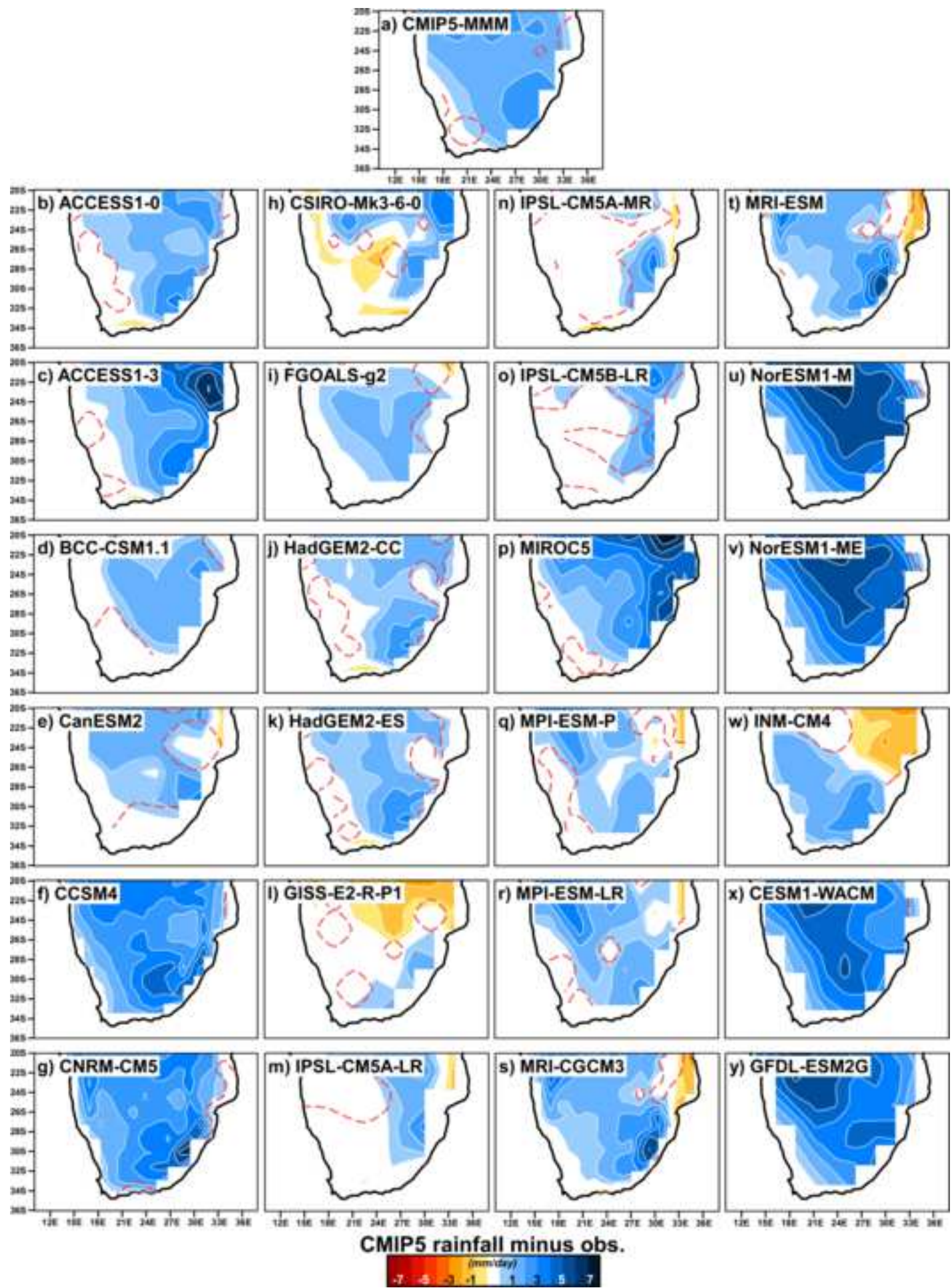


Figure 3
[Click here to download high resolution image](#)

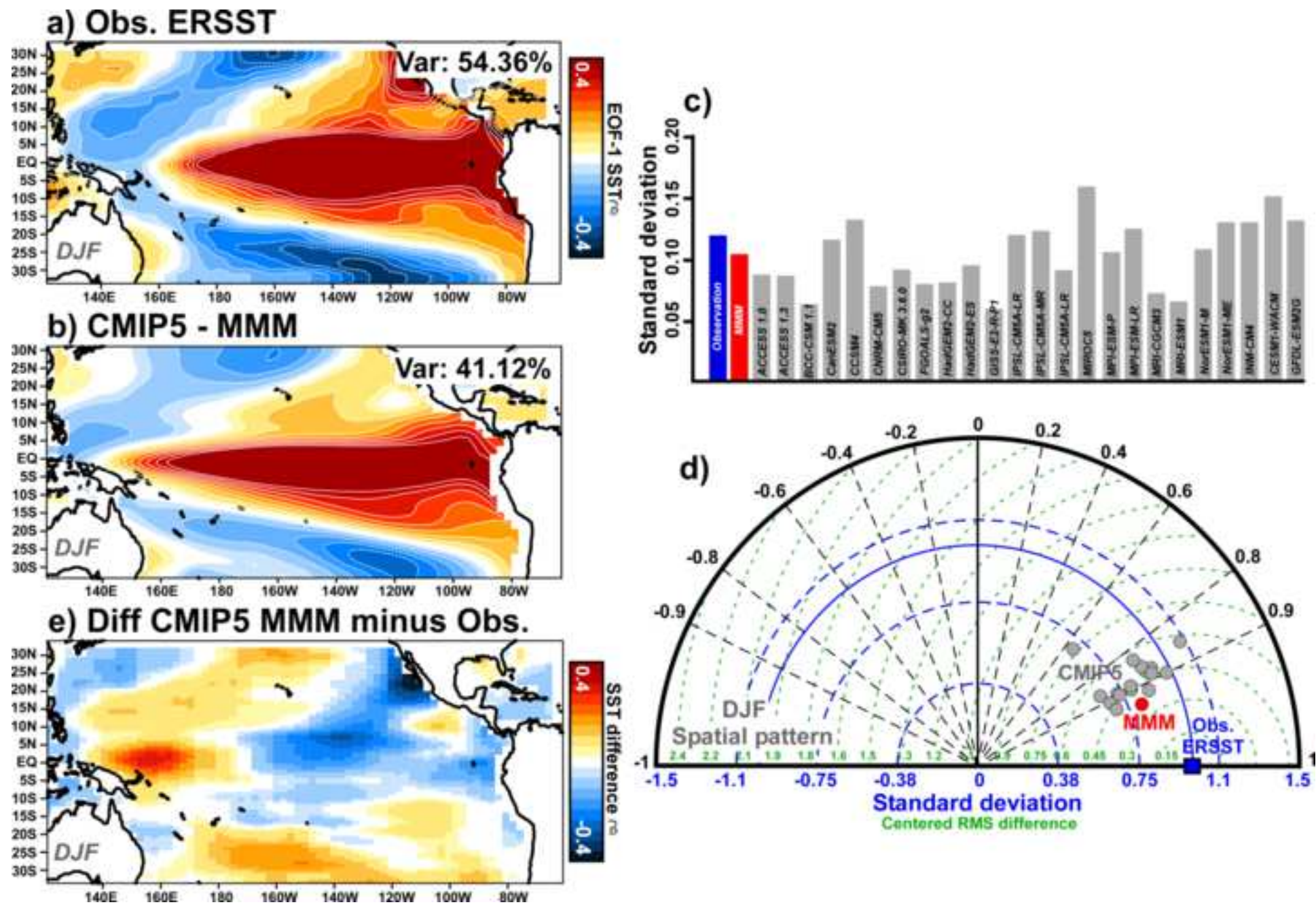


Figure 4
[Click here to download high resolution image](#)

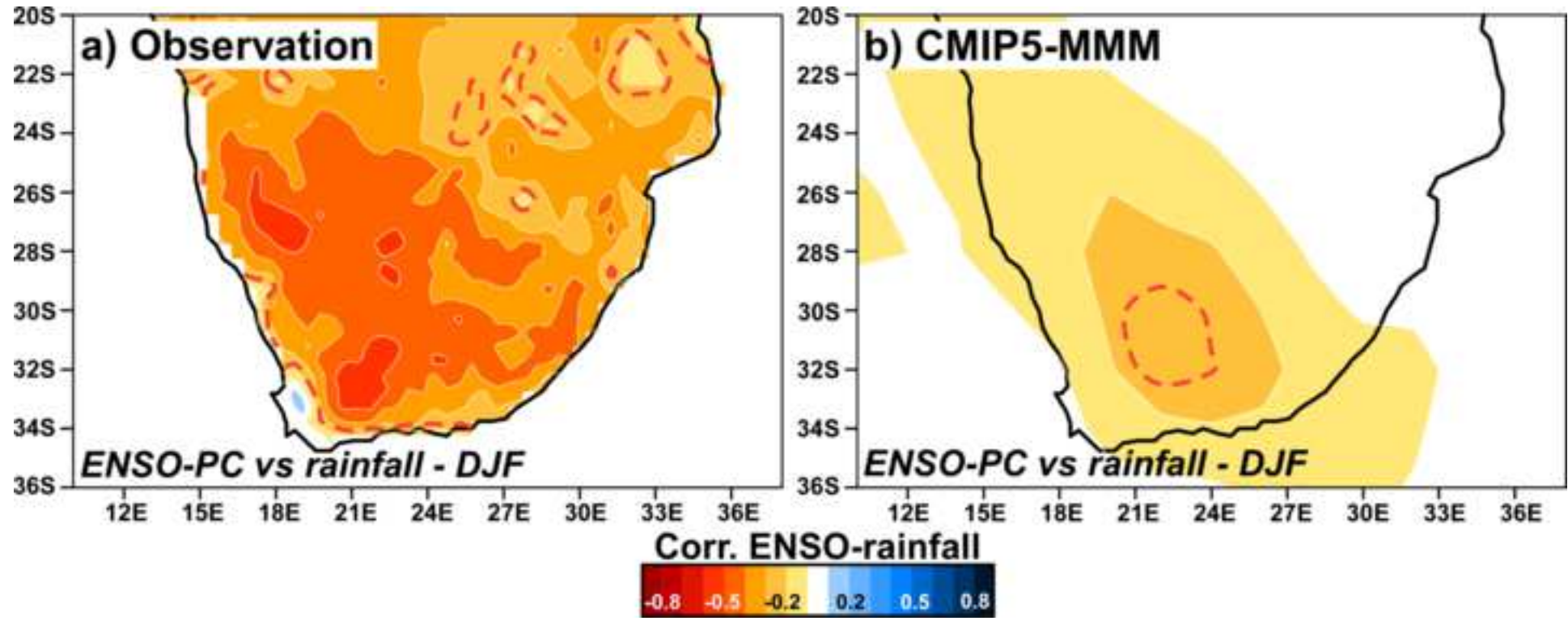


Figure 5
[Click here to download high resolution image](#)

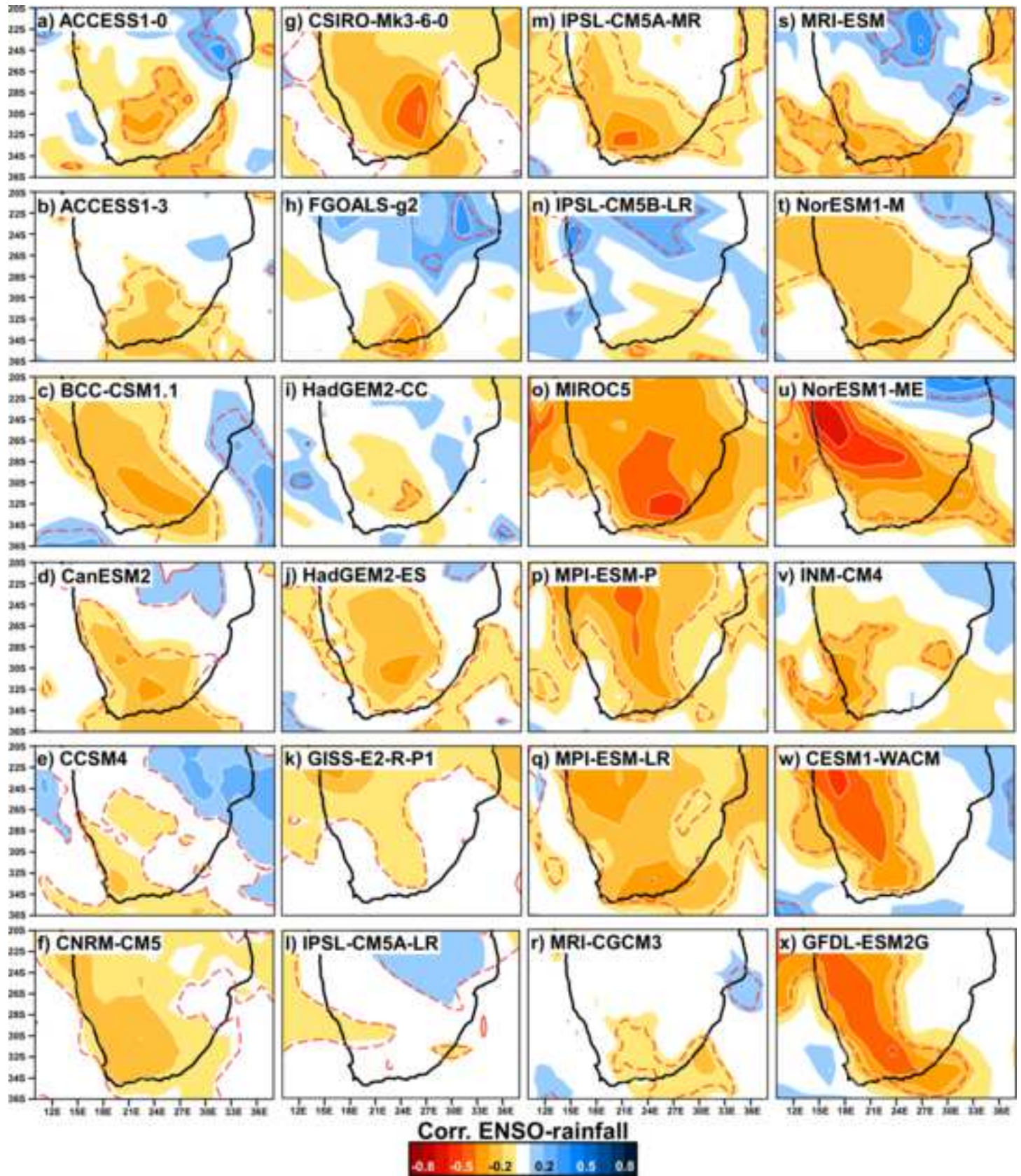


Figure 6
[Click here to download high resolution image](#)

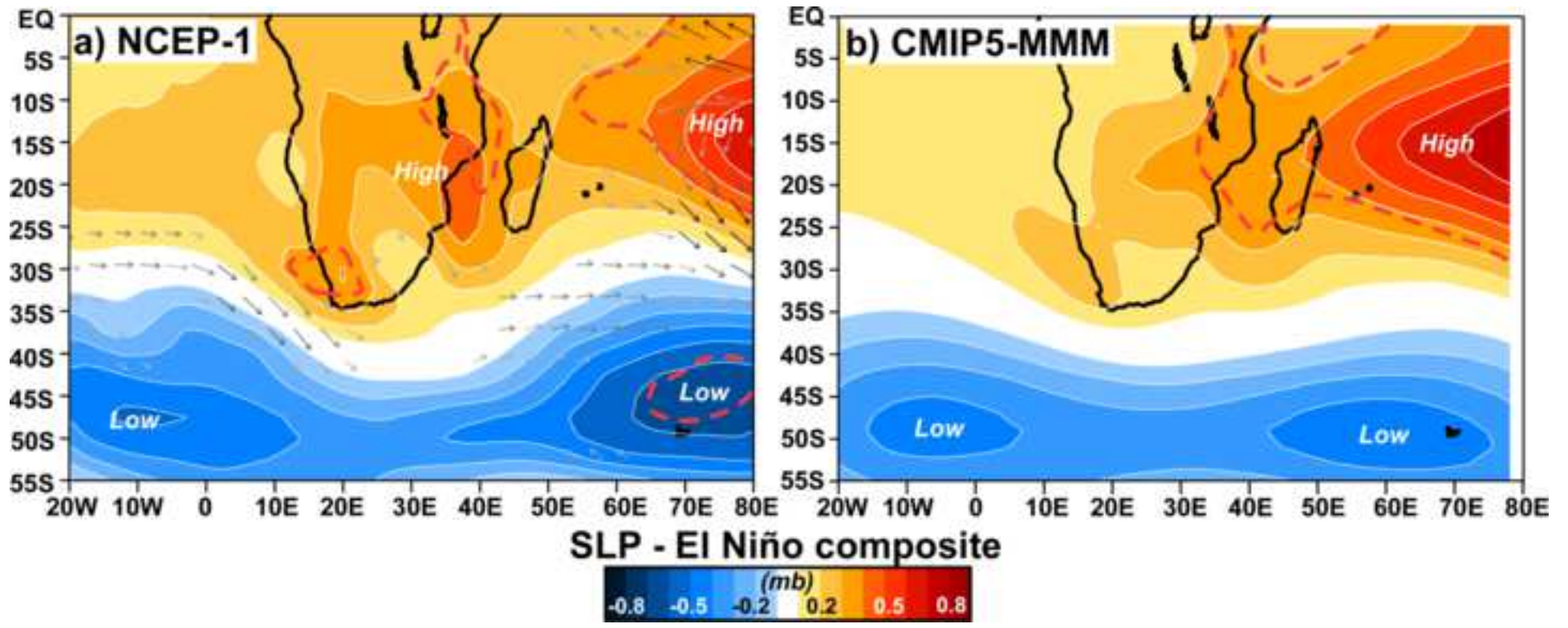


Figure 7

[Click here to download high resolution image](#)

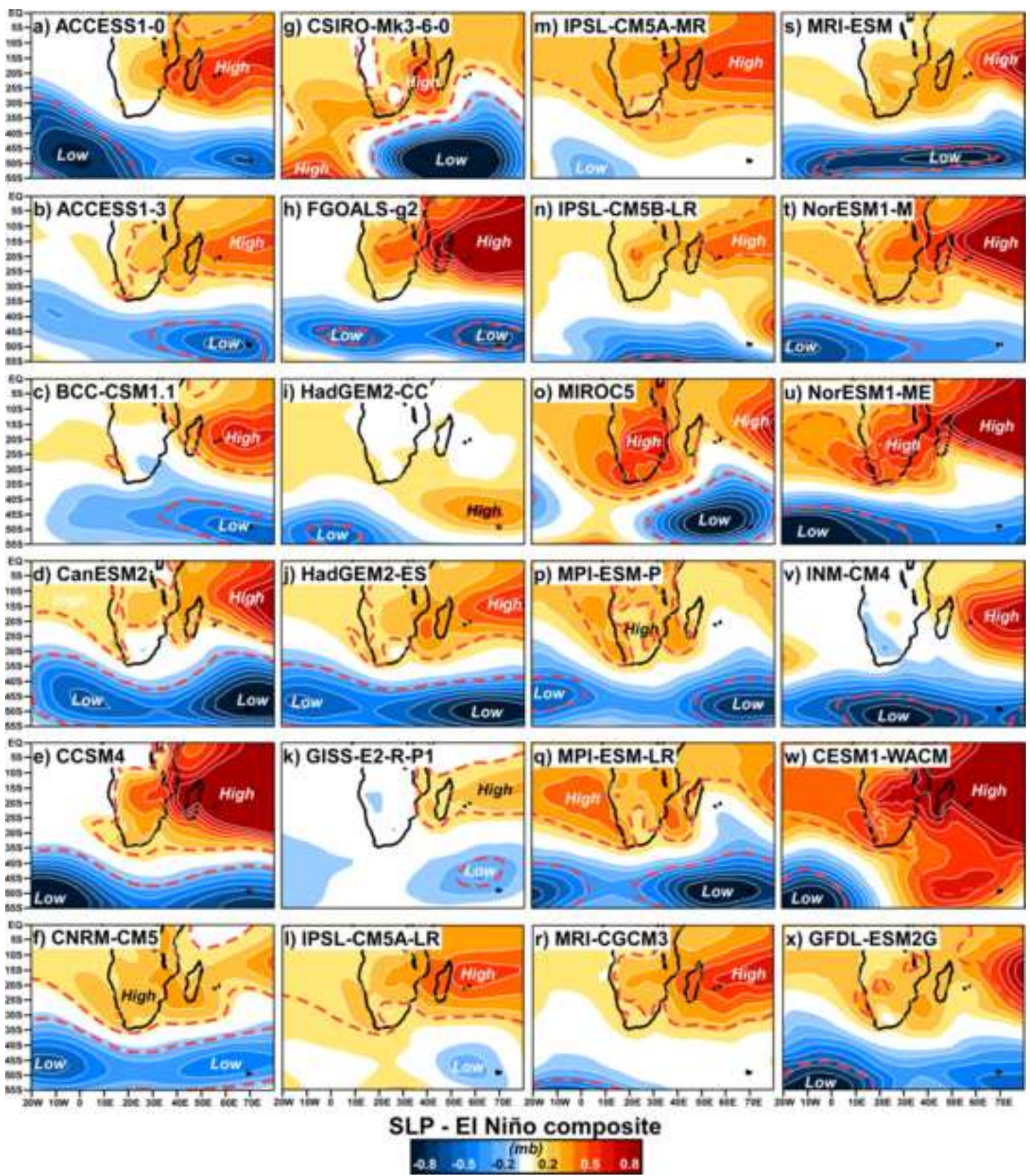


Figure 8
[Click here to download high resolution image](#)

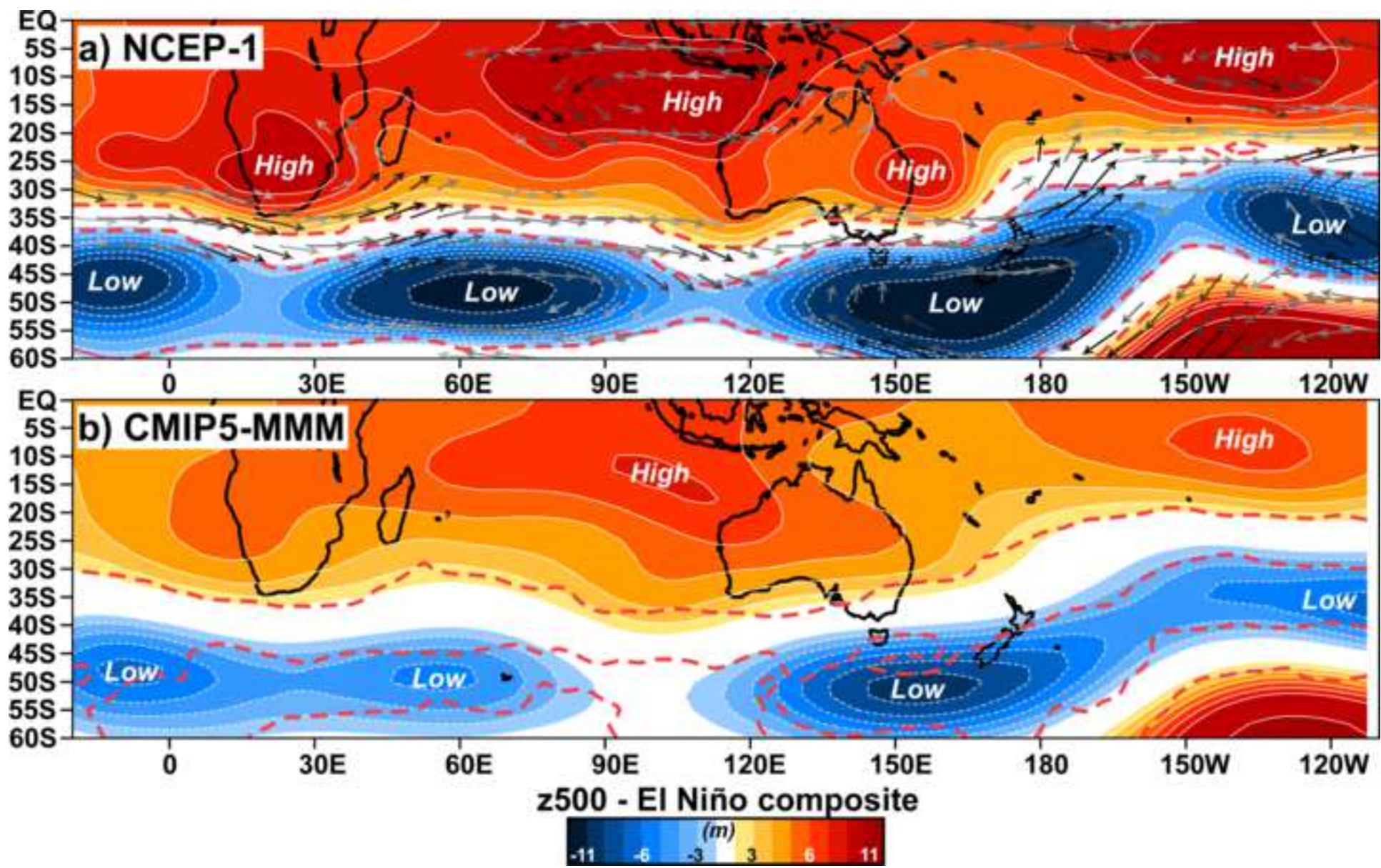


Figure 9
[Click here to download high resolution image](#)

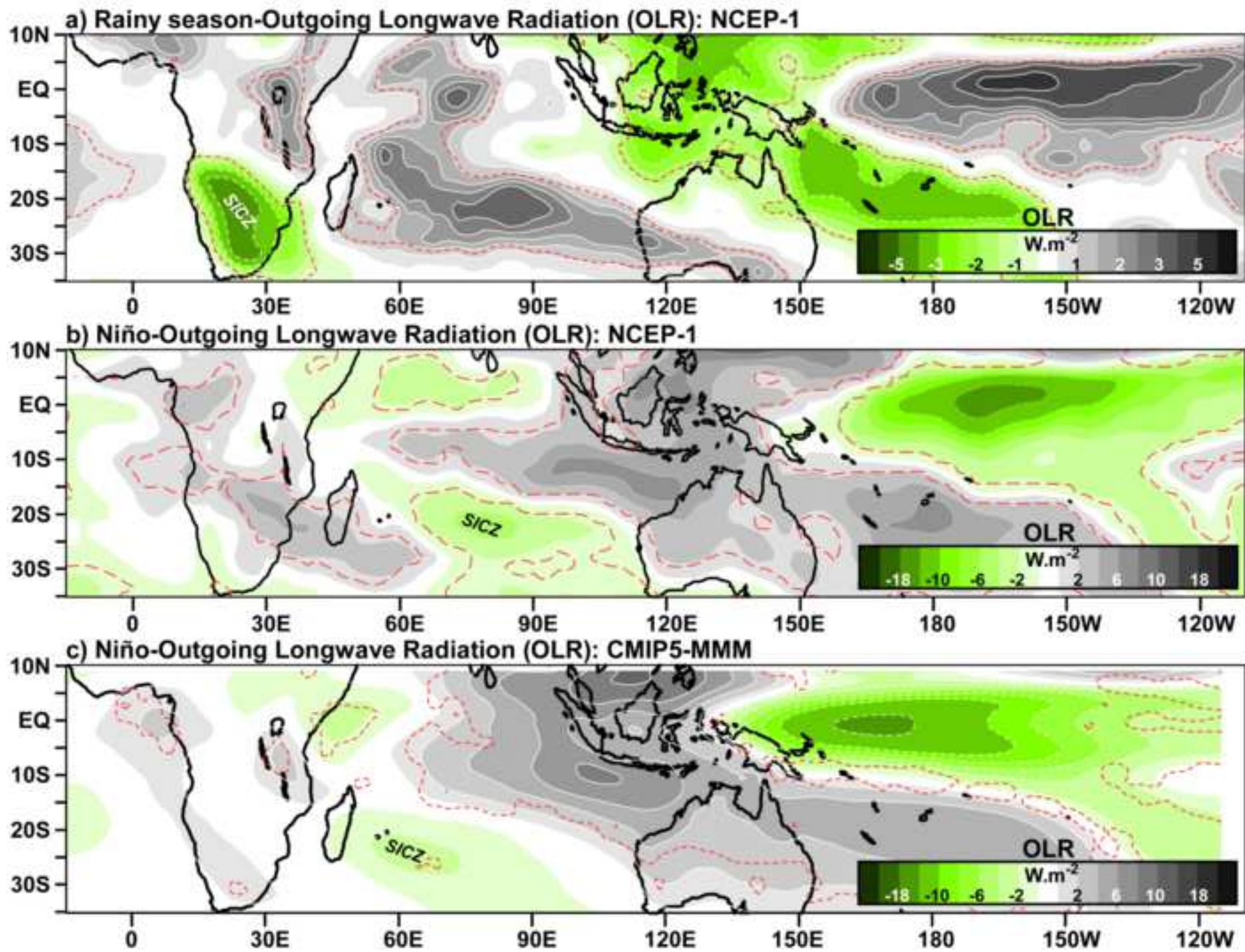
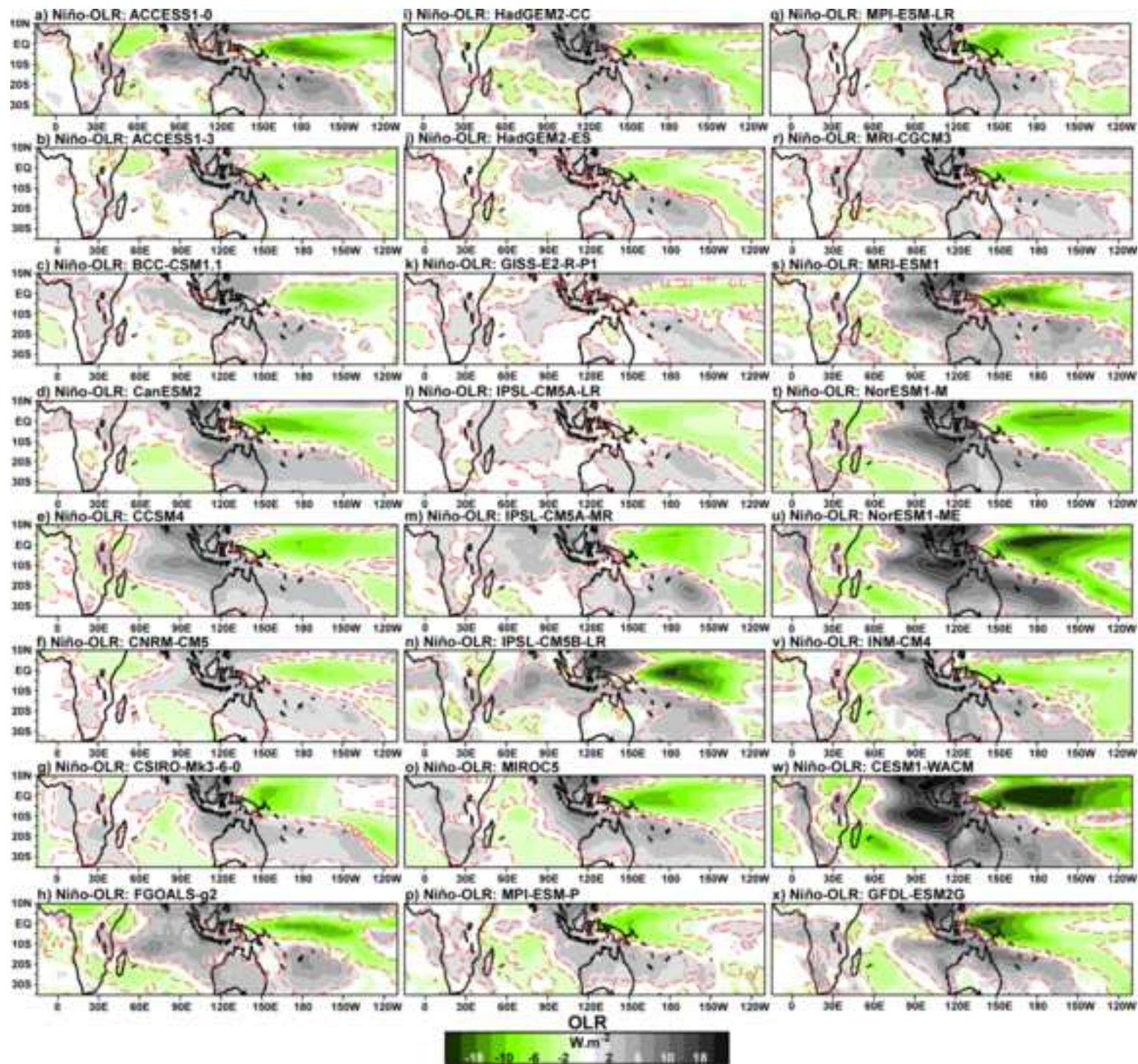
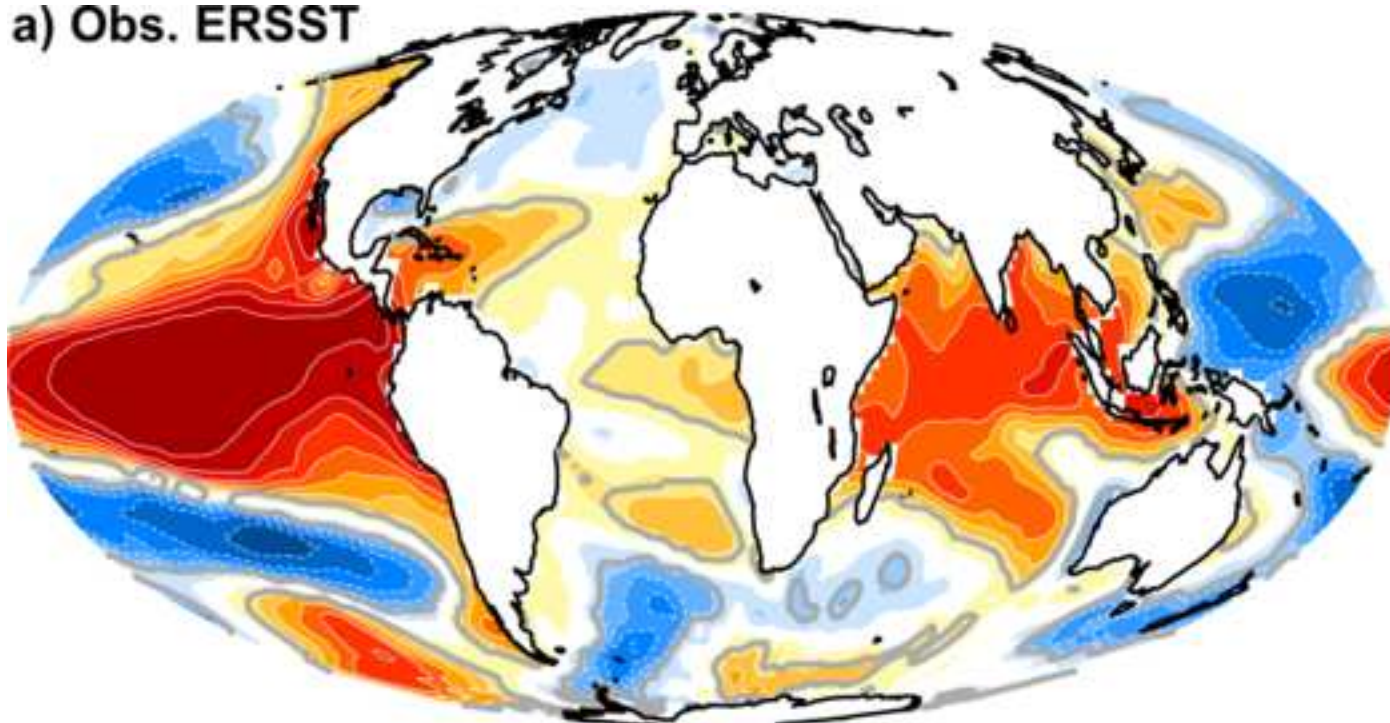


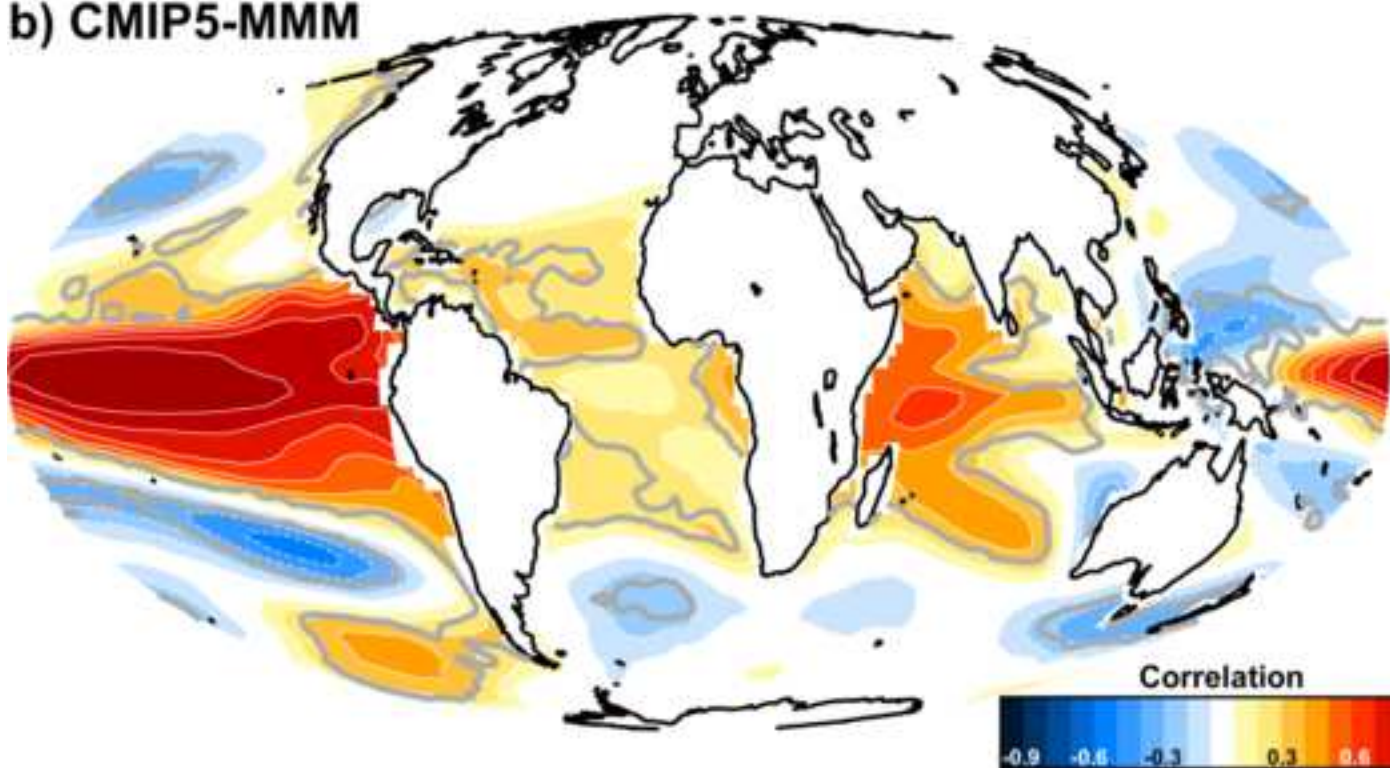
Figure 10
[Click here to download high resolution image](#)



a) Obs. ERSST



b) CMIP5-MMM



Correlation

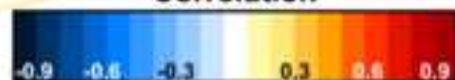


Figure 12
[Click here to download high resolution image](#)

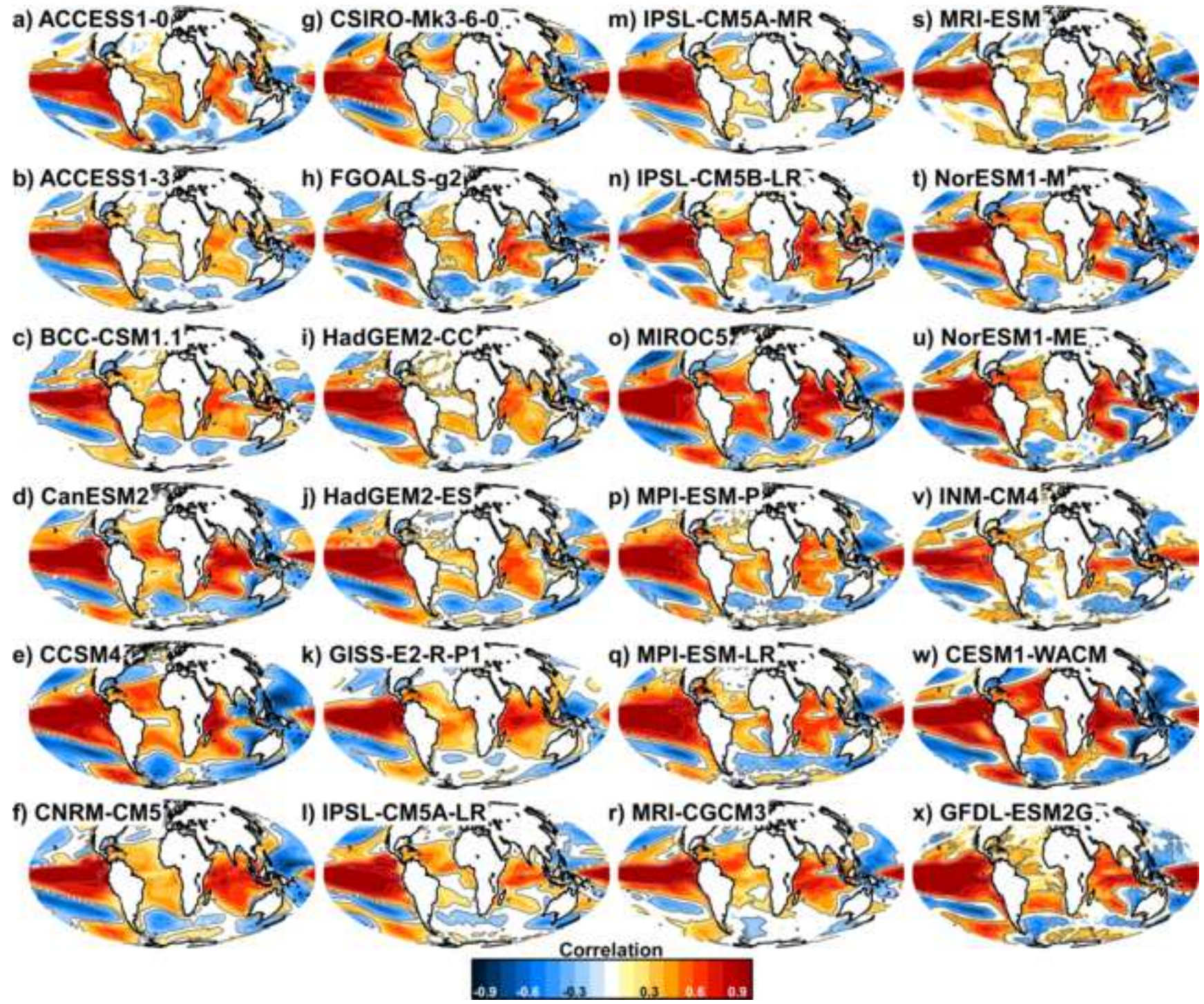


Figure 13
[Click here to download high resolution image](#)

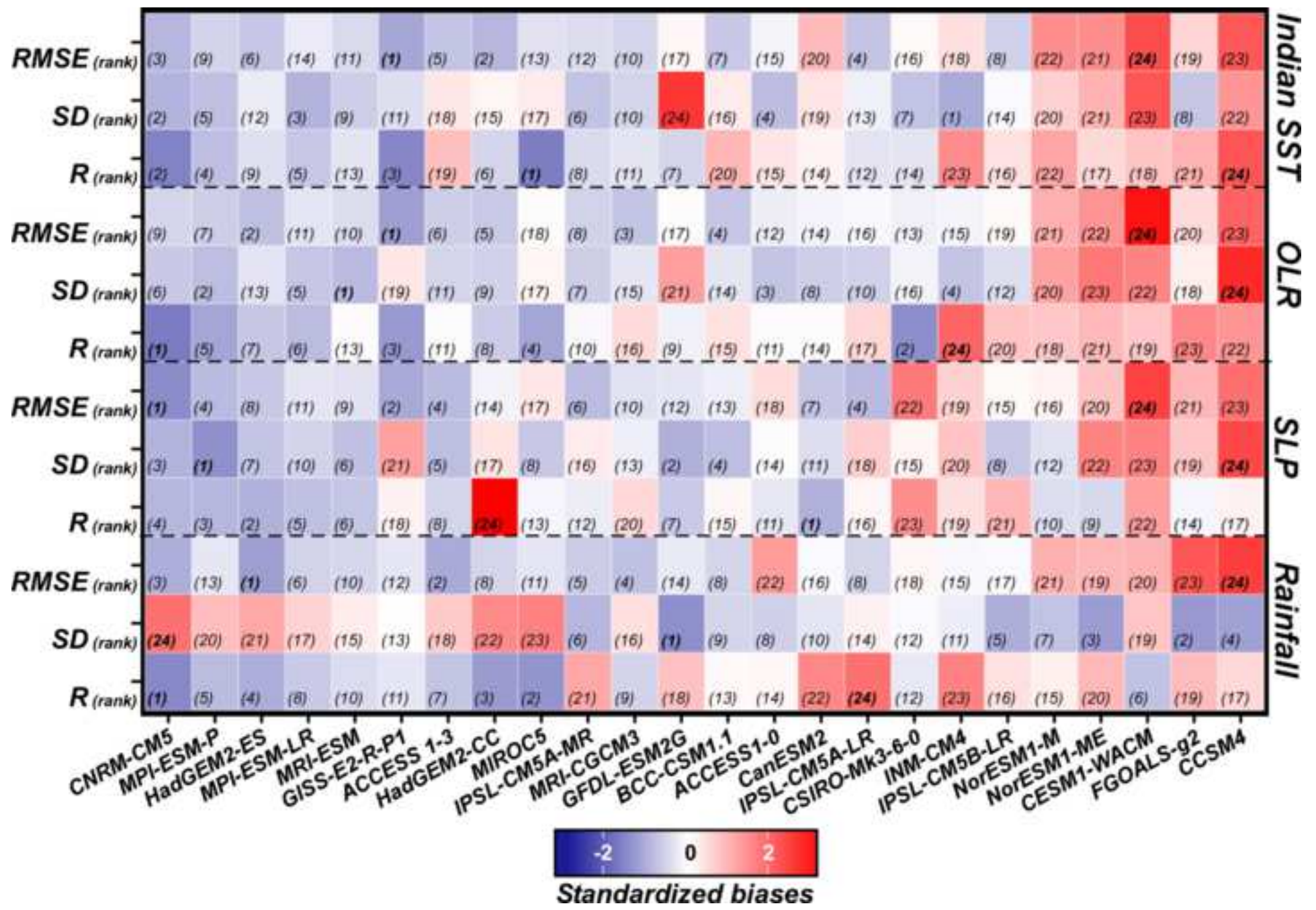


Table 1
[Click here to download high resolution image](#)

	Institution	Variables	Name <i>(ens. member)</i>	Period
Obs.	CRU, <i>United Kingdom</i>	pr	CRU TS 3.21	1950-2005
	NOAA/NCDC, <i>USA</i>	sst	ERSST v3b	1950-2005
	NCEP/NCAR, <i>USA</i>	slp, U, V, z500, OLR	NCEP-1	1950-2005
CMIP5 models	CSIRO/BOM, <i>Australia</i>	pr, sst, slp, z500, OLR	ACCESS 1.0 ⁽¹⁾	1950-2005
	CSIRO/BOM, <i>Australia</i>	pr, sst, slp, z500, OLR	ACCESS 1.3 ⁽³⁾	1950-2005
	BCC, <i>China</i>	pr, sst, slp, z500, OLR	BCC-CSM1.1 ⁽³⁾	1950-2005
	CCCma, <i>Canada</i>	pr, sst, slp, z500, OLR	CanESM2 ⁽⁵⁾	1950-2005
	NCAR, <i>USA</i>	pr, sst, slp, z500, OLR	CCSM4 ⁽⁶⁾	1950-2005
	CNRM/CERFACS, <i>France</i>	pr, sst, slp, z500, OLR	CNRM-CM5 ⁽¹⁰⁾	1950-2005
	CSIRO/QCCCE, <i>Australia</i>	pr, sst, slp, z500, OLR	CSIRO-MK3.6.0 ⁽¹⁰⁾	1950-2005
	LASG/CESS, <i>China</i>	pr, sst, slp, z500, OLR	FGOALS-g2 ⁽¹⁾	1950-2005
	MOHC, <i>United Kingdom</i>	pr, sst, slp, z500, OLR	HadGEM2-CC ⁽²⁾	1950-2005
	MOHC, <i>United Kingdom</i>	pr, sst, slp, z500, OLR	HadGEM2-ES ⁽⁴⁾	1950-2005
	NASA GISS, <i>USA</i>	pr, sst, slp, z500, OLR	GISS-E2-R-P1 ⁽⁶⁾	1950-2005
	IPSL, <i>France</i>	pr, sst, slp, z500, OLR	IPSL-CM5A-LR ⁽⁶⁾	1950-2005
	IPSL, <i>France</i>	pr, sst, slp, z500, OLR	IPSL-CM5A-MR ⁽³⁾	1950-2005
	IPSL, <i>France</i>	pr, sst, slp, z500, OLR	IPSL-CM5B-LR ⁽¹⁾	1950-2005
	MIROC, <i>Japan</i>	pr, sst, slp, z500, OLR	MIROC5 ⁽⁵⁾	1950-2005
	MPI-M, <i>Germany</i>	pr, sst, slp, z500, OLR	MPI-ESM-P ⁽²⁾	1950-2005
	MPI-M, <i>Germany</i>	pr, sst, slp, z500, OLR	MPI-ESM-LR ⁽³⁾	1950-2005
	MRI, <i>Japan</i>	pr, sst, slp, z500, OLR	MRI-CGCM3 ⁽³⁾	1950-2005
	MRI, <i>Japan</i>	pr, sst, slp, z500, OLR	MRI-ESM1 ⁽¹⁾	1950-2005
	NCC, <i>Norway</i>	pr, sst, slp, z500, OLR	NorESM1-M ⁽³⁾	1950-2005
	NCC, <i>Norway</i>	pr, sst, slp, z500, OLR	NorESM1-ME ⁽¹⁾	1950-2005
	INM, <i>Russia</i>	pr, sst, slp, z500, OLR	INM-CM4 ⁽¹⁾	1950-2005
	NSF/DOE/NCAR, <i>USA</i>	pr, sst, slp, z500, OLR	CESM1-WACM ⁽¹⁾	1950-2005
NOAA GFDL, <i>USA</i>	pr, sst, slp, z500, OLR	GFDL-ESM2G ⁽¹⁾	1950-2005	